Chem Soc Rev

REVIEW ARTICLE

View Article Online
View Journal | View Issue

Cite this: *Chem. Soc. Rev.*, 2022, **51**, 628

Electronic structure and bonding in endohedral Zintl clusters

John E. McGrady, †*[a] Florian Weigend †*[b] and Stefanie Dehnen †*[b]

Endohedral Zintl clusters—multi-metallic anionic molecules in which a d-block or f-block metal atom is enclosed by p-block (semi)metal atoms—are very topical in contemporary inorganic chemistry. Not only do they provide insight into the embryonic states of intermetallic compounds and show promise in catalytic applications, they also shed light on the nature of chemical bonding between metal atoms. Over the past two decades, a plethora of endohedral Zintl clusters have been synthesized, revealing a fascinating diversity of molecular architectures. Many different perspectives on the bonding in them have emerged in the literature, sometimes complementary and sometimes conflicting, and there has been no concerted effort to classify the entire family based on a small number of unifying principles. A closer look, however, reveals distinct patterns in structure and bonding that reflect the extent to which valence electrons are shared between the endohedral atom and the cluster shell. We show that there is a much more uniform relationship between the total valence electron count and the structure and bonding patterns of these clusters than previously anticipated. All of the p-block (semi)metal shells can be placed on a ladder of total valence electron count that ranges between **4*n*+2** (*closo* deltahedra), **5*n*** (closed, three-bonded polyhedra) and **6*n*** (crown-like structures). Although some structural isomerism can occur for a given electron count, the presence of a central metal cation imposes a preference for rather regular and approximately spherical structures which maximise electrostatic interactions between the metal and the shell. In cases where the endohedral metal has relatively accessible valence electrons (from the d or f shells), it can also contribute its valence electrons to the total electron count of the cluster shell, raising the effective electron count and often altering the structural preferences. The electronic situation in any given cluster is considered from different perspectives, some more physical and some more chemical, in a way that highlights the important point that, in the end, they explain the same situation. This article provides a unifying perspective of bonding that captures the structural diversity across this diverse family of multimetallic clusters.

Received 16th August 2021

DOI: 10.1039/d1cs00775k

rsc.li/chem-soc-rev

1. Introduction

1.1 Multimetallic clusters

Progress in (semi)metal cluster chemistry has been made on a number of fronts over the past few decades, and the field has seen major advances in synthesis, characterisation, and also materials chemistry.[1–23] Multimetallic clusters may be viewed as embryonic states of intermetallic phase formation, and as such represent discrete molecular models that offer insight into the broad spectrum of chemical bonding between metal atoms. They are, however, much more than an appealing playground for theory: they can also be used as precursors to new (multi-)metallic solids as well as showing potential in bond-activation reactions.[24–31]

The majority of experimental papers on multimetallic clusters are now complemented by theory, the broad aim of which is to rationalise structure and reactivity. The very fact that these clusters are of interest to both chemistry and physics communities makes it inevitable that different approaches to electronic structure have been adopted, using different methodologies and different scientific language to reflect the interests and priorities of the particular research teams. Whilst this diversity of perspectives has undoubtedly enhanced our understanding of the bonding, the rather different approaches have had the unfortunate side effect of obscuring important links between different classes of compound. A close inspection of the many reported examples reveals important repeating patterns that allow a classification of the known landscape into a few connected cluster families. It is the purpose of this review

[a] *Physical and Theoretical Chemistry Laboratory, Department of Chemistry, University of Oxford, South Parks Road, OX1 3QZ, UK. E-mail: john.mcgrady@chem.ox.ac.uk*
[b] *Fachbereich Chemie and Wissenschaftliches Zentrum für Materialwissenschaften, Philipps University Marburg, Hans-Meerwein-Straße 4, 35043 Marburg, Germany. E-mail: florian.weigend@chemie.uni-marburg.de, dehnen@chemie.uni-marburg.de*
† All three authors contributed equally and co-wrote the article.

to explore the underlying relationships between so-called endohedral Zintl clusters, the electronic properties of which have been interpreted in many different ways, and to set out a framework for understanding the common features that link this fascinating class of compounds.

1.2 Endohedral Zintl clusters: the impact of interstitial atoms

Our focus in this review will be firmly on endohedral Zintl clusters[32–37] that are primarily the domain of synthetic inorganic chemistry and, very recently, materials science, but they have also been the subject of many theoretical and gas-phase spectroscopic studies.[38–52] Generally, Zintl clusters are anionic molecules made up of atoms from p-block (semi)metals. More specifically, the title of this article narrows the focus further to endohedral clusters, in which a single atom or ion of the d- or f-block elements is encapsulated within a cluster shell comprising a much larger number of p-block (semi)metal atoms from groups 13 to 15. A classic examples of this kind would be $[Pt@Pb_{12}]^{2-}$,[53] where the '@' symbol is used to indicate endohedral encapsulation. Whilst the stability of these clusters is generally reliant on the presence of the metal in the sense that the corresponding 'empty' clusters do not exist (the exception being Pb_{10}^{2-}), this does not necessarily mean that entirely different bonding models are required for homo- and heterometallic cases – by contrast, the concepts that have been developed for simple molecules and empty clusters of lighter atoms generally apply here, too. The critical question that we need to address is what is the role of the d or f electrons on the endohedral atom? We can easily identify some limits to the range of possible answers to this question. On the one hand, it is possible that the d/f electrons are entirely core-like and do not interact with the orbitals on the cage (the 'non-interacting limit'). At this extreme, the endohedral atom is effectively acting as a noble gas atom trapped inside a cage only by the very large activation barrier required to pass through the walls; here, its role is that of a mere structural template, much like in the noble gas clathrates,[54–57] for instance. At the opposite extreme, the endohedral metal could transfer all of its valence electrons to cage, which might then adopt a structure that reflects the presence of additional electron density in its frontier orbitals (the 'fully-interacting limit'). In such cases, there are obvious analogies to back bonding in classic organometallic complexes: the presence of low-lying vacant orbitals on the cluster shell allows it to act, in effect, as an acceptor ligand. In between these two limits is a continuum of possibilities linked by different degrees of covalency, where the electrons are shared between inner metal and cage atoms. Within this continuum, we find examples where the cluster

John E. McGrady

John McGrady studied for his first degree at the University of Oxford before a PhD at the Australian National University. Following postdoctoral positions at Imperial College, the Australian National University and the Université de Montpellier II in France, he was appointed to a lectureship at the University of York. He then moved to the University of Glasgow as a WestCHEM chair, before taking his current position as Professor of Computational Inorganic Chemistry at the University of Oxford in 2009. He is a fellow at New College, Oxford. His research interests are in computational inorganic chemistry, with a particular focus on the structure and reactivity of cluster compounds.

Florian Weigend

Florian Weigend received his PhD from the University of Karlsruhe, now Karlsruhe Institute of Technology (KIT) and became a group leader at the Institute of Nanotechnology at KIT. Currently he is head of the Applied Quantum Chemistry unit at Philipps-Universität Marburg with focus on quantum chemistry of inorganic systems. He is a core developer of the quantum chemistry suite TURBOMOLE.

Stefanie Dehnen

Stefanie Dehnen obtained her diploma in 1993 and her doctoral degree in 1996 from the University of Karlsruhe (KIT). After a postdoctoral stay in theoretical chemistry (1997) she completed her Habilitation in inorganic chemistry in 2004. As of 2006 she has been Full Professor of Inorganic Chemistry at Philipps-Universität Marburg. She is a full member of the European Academy of Sciences (EurASc) and of Leopoldina German National Academy of Sciences. She is the 2022 recipient of the Gottfried Wilhelm Leibniz Prize awarded by the German Research Foundation (DFG). Her current research is focused on the synthesis and experimental as well as quantum chemical investigation of compounds with multinary, in particular multimetallic, molecular nano-architectures, which possess potential as innovative catalysts, white-light emitters, or battery materials.

is only slightly distorted from the structure that we might have expected at the 'non-interacting' limit whereas in others we find a gross rearrangement to an entirely different structural type. We also find cases where the metal atom shell supports radical character (*i.e.* unpaired electron density), precisely as extended aromatic ligands do in many transition metal complexes. The diverse family of endohedral Zintl clusters therefore provides a uniquely rich platform for exploring different classes of chemical bonding. Ultimately, a close interplay between experiment and theory will be required to fully understand the chemistry of this intriguing family of clusters. In this review we will, for the most part, use examples of clusters with 12-vertex atoms to illustrate the key points, simply because this family is the most diverse, although we also bring in examples with other vertex counts.

1.3 The correlation between valence electron count and structural features of simple metal clusters: early considerations and modern views.

The simplest cases of metal clusters, prominent examples of which are found in polyanions of group 15 (semi)metals like Sb_7^{3-} or Bi_{11}^{3-}, can be understood simply in terms of the 8 – N rule: each atom with a well-defined number of valence electrons, N, forms 8 − N 2-centre-2-electron (2c–2e) bonds to neighbouring atoms to complete its octet. Such clusters have $5n$ valence electrons and form the most symmetric cages that can be generated with the given number of three-bonded atoms. By contrast, clusters that are formally electron-deficient cannot be understood in terms of 2c–2e bonds. At a minimum number of $4n + 2$ valence electrons, such as found in group 14 anions like Sn_5^{2-} or Pb_{10}^{2-}, they form spherical 'closed' deltahedral cages reminiscent of the (isoelectronic) boranes.[58]

The seminal work of Wade and Mingos and Lipscomb in the 1970s that formulated a simple set of rules to account for structural trends across deltahedral clusters of different vertex count,[59–62] and the later contributions of Mingos and Jemmis to this field,[63–71] represent major landmarks in the sense that they brought order to an extensive body of structural data. It is remarkable how well these rules also apply to iso-valence-electronic p-block metal clusters. It is important to emphasise that much of the important insight from this early work emerged from relatively simple theoretical models—primarily a combination of symmetry-based arguments and tight-binding approaches such as the extended Hückel methodology pioneered by the Hoffmann school.[72] These tools did not allow for the calculation of the total energy, let alone gradients, and so all of the very profound advances in this period came about without access to optimised geometries. In the modern age of density functional theory (DFT) and fast computers, many papers begin and sometimes also end with a set of optimised geometries, and the lesson we can learn from the work of Wade, Mingos and others is that it is the patterns and trends within these data, rather than the data themselves, which have real value. Moreover, these patterns should transcend the differences in methodology that complicate the comparison of different reports, particularly within the DFT literature. At the same time as the chemistry community was applying tight-binding models to these problems, the physics community took an alternative path, making extensive use of the jellium model to interpret the properties of small, typically gas-phase, clusters.[73–75] The jellium model is also closely linked to ideas of shape and symmetry, although 'shape' in this sense relates to the approximate sphericality of the cluster, rather than the connectivity of individual vertices. The fact that the jellium model is, in some sense, less dependent on knowledge of precise atomic positions makes it a natural partner to gas-phase spectroscopy, where structural information can only be inferred from the interpretation of electronic, vibrational or rotational signatures. Closely linked to the jellium model is the concept of a 'superatom' pioneered by Castleman and others:[76–82] the simple idea here is that closed electron shells in clusters mimic the well-defined atomic shells that give rise to Mendeleev's iconic periodic table of the elements. Some of the most famous endohedral 'superatoms' – albeit with an interstitial p-block metal atom – are Al_{13}^- (= $[Al@Al_{12}]^-$), and its isoelectronic analogues $[B@Al_{12}]^-$, $[Si@Al_{12}]$ and $[P@Al_{12}]^+$, which have been studied intensely using both spectroscopy and theoretical methods.[37] All three have the 'magic' number of 40 valence electrons that corresponds to a shell closure and, as illustrated in Fig. 1, they have perfectly icosahedral structures and large HOMO–LUMO gaps. In contrast, clusters with higher or lower electron counts are distorted away from icosahedral symmetry and have substantially smaller HOMO–LUMO gaps.[78]

The rather diverse array of theoretical models that have been used over the years is perhaps an inevitable reflection of the fact that cluster chemistry spans the traditional disciplines of inorganic chemistry, physical chemistry, physics itself and, most recently, materials science. We believe that many important links between clusters of different types have been obscured by differences in methodology, language and terminology used by different groups. Our aim in this review is to explore these links and cut through methodological issues

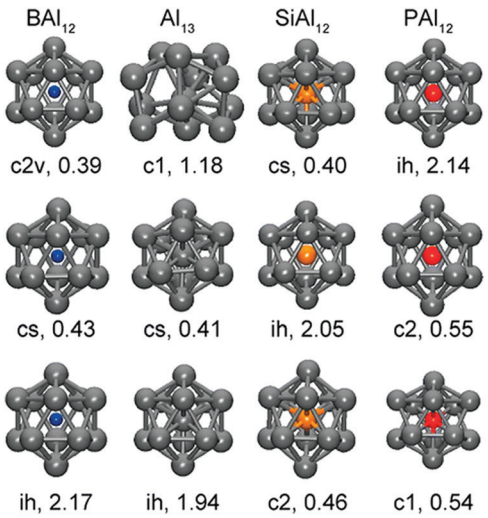

Fig. 1 Optimized structures of 'superatoms' $[M@Al_{12}]^q$ (X = B, Al, Si, and P) with q = +1 (top), q = 0 (centre), and q = −1 bottom. The symmetry and HOMO–LUMO gaps (eV) are also shown. This figure has been reproduced from ref. 78 with permission from ACS, copyright 2013).

to identify the important periodic trends that that control bonding in these clusters.

2. Endohedral Zintl clusters in experiment and theory

In this section we will present a brief overview of the most important experimental techniques that find use in the Zintl cluster field and the possible applications of the clusters. This is followed by an outline of the key theoretical methods that have been used to analyse their properties.

2.1 Synthetic access of endohedral Zintl clusters

It is not our purpose here to present a detailed introduction into Zintl cluster synthesis and characterization because this has been reviewed extensively elsewhere in recent times.[15,19,32,36] However, a few brief comments are necessary to give context to the subsequent discussion of structure and bonding, while we refer the interested reader to the literature for more detailed information.

The most common approach to the synthesis of compounds containing endohedral Zintl clusters starts out from 'Zintl salts', *i.e.*, compounds comprising sequestrated cations for the compensation of the anions' charge (Scheme 1, top).

In the vast majority of cases, the cation is $[K(crypt\text{-}222)]^+$ (crypt-222 = 4,7,13,16,21,24-hexaoxa-1,10-diazabicyclo-[8.8.8]hexacosane), favoured because of its superior ability to drive the crystallization of the large (and approximately spherical) cluster anions. However, some publications have also reported the use of mixtures of $[K(crypt\text{-}222)]^+$ with unsequestrated K^+ ions. Such salts are typically significantly soluble at room-temperature in highly polar solvents like ethane-1,2-diamine (en), liquid NH_3, dimethylformamide (DMF), or pyridine (py), and so allow for wet-chemical reactions with d- or f-block organometallics or coordination compounds. This method works particularly well for ternary Zintl clusters that are obtained in reactions of salts of binary Zintl anions like $(InBi_3)^{2-}$ or $(Sn_2Sb_2)^{2-}$. A variation of this method involves the use of pristine Zintl phases, *i.e.*, intermetallic compounds without cation sequestration like K_4Ge_9, $K_{12}Si_{17}$, or K_5Bi_4, which are extracted *in situ* into the solvent of choice (including liquid ammonia) in the presence of the cation-sequestration agent, and subsequently reacted with the d-/f-block metal compounds. In both cases, the products are relatively soluble salts of anionic Zintl clusters (Scheme 1, centre). An alternative strategy, which avoids the use of solvents, is solid state synthesis at high temperatures. The resulting compounds are typically ternary alloys, in which the Zintl clusters may carry much higher anionic charges and, as a consequence, typically have lower solubility (Scheme 1, bottom).

Solution reactions starting from *Zintl* salts

$[A(seq)]_aE_b + c\,[ML_n]$ or $[A(seq)]_aE^1{}_bE^2{}_c + c\,[ML_n]$ → (1) + *solv*; (2) *workup* → $[A(seq)]_x[M_m@E^1{}_yE^2{}_z]$

Solution reactions starting from *Zintl* phases

$A_aE_b + c\,[ML_n]$ or $A_aE^1{}_bE^2{}_c + c\,[ML_n]$ → (1) + *solv* / + *seq*; (2) *workup* → $[A(seq)]_x[M_m@E^1{}_yE^2{}_z]$

Solid-state reactions followed by extraction

a A + b E + c M or $A_aE_b + c\,M$ or $A_aE^1{}_bE^2{}_c + c\,M$ → 1) ΔΔ; 2) + *solv* / + *seq*; 3) *workup* → $[A(seq)]_x[M_m@E^1{}_yE^2{}_z]$

A = alkali(ne earth) metal, typically K; *L* = complex ligand
M = transition metal, lanthanide, actinide; E, E^1, E^2 = p-block (semi)metals from groups 13-15
E^1, E^2 = p-block (semi)metals
seq = sequestration agent: 4,7,13,16,21,24-hexaoxa-1,10-diazabicyclo[8.8.8]hexacosane (crypt-222) or 1,4,7,10,13,16-hexaoxacyclooctadecan (18-crown-6)
solv = solvent: ethane-1,2-diamine (en), liquid NH_3, dimethylformamide (DMF), pyridine (py)
workup = filtration, layering (e.g., with toluene)

Scheme 1 General synthetic approaches to endohedral, anionic Zintl clusters of the general formula $[M_m@E_x^1E_y^2]^{q-}$ by reacting Zintl salts (top) or pristine binary or ternary alloys (centre) with transition metal complexes, or by high-temperature treatment of the desired components starting out from different solid precursors (bottom). Note that the generalized product formula does not account for endohedral clusters that bind a few external organic or elementorganic ligands, some of which have been reported.

2.2 Experimental characterization of endohedral Zintl clusters.

The experimental characterization and further analysis of these compounds is generally done with X-ray diffraction for structure elucidation, often in combination with micro-X-ray fluorescence (μ-XRF) or energy-dispersive X-ray (EDX) spectroscopy to identify or corroborate the heavy-atom composition of the compounds.

If the solubility of the salts and the stability of the anions permits, mass spectrometry has proven to be a valuable tool for very precise identification of anion composition, though it is important to emphasise that the transfer to the gas phase is usually accompanied by oxidation to lower-charge anions, and may also lead to fragmentation of the clusters. As a result, inferences about the composition of condensed phases from the analysis of mass spectrometric data must be done with some caution. In some cases complementary studies on solid samples or solutions using magnetometry or NMR, EPR, Mößbauer and infra-red/Raman spectroscopies have offered important insights into features like the protonation state of clusters, their solution dynamics, the metals' valence states, or the magnetic ground states. These complementary methods are particularly important in cases where the interpretation of X-ray diffraction data is ambiguous, for example when clusters contain neighbouring elements in the periodic table with similar scattering factors, when extensive disorder of approximately spherical clusters complicates the structure determination, or when the cationic components cannot be localized from the structural data, leaving the total charge on the anionic component undetermined. Whilst the synergy between these different experimental techniques is obvious, it is only when combined with theory that the full information content of the data emerges. It is this synergy between experiment and theory that we emphasise throughout this article.

2.3 Chemical properties and potential use of Zintl clusters

Zintl clusters stand out not only for their structural aesthetics and their often remarkable bonding characteristics, which are

the main scope of this review article, but also for their potential to display properties that may prove useful in future applications. The multitude of possible combinations of (semi)metal atoms in Zintl clusters means that properties such as reactivity and solubility can be finely tuned across a broad spectrum, with many important consequences. The most obvious of these is that the combination of reactivity and solubility determines the feasibility of being able to characterize and analyse a species and, ultimately, whether it is amenable to isolation. In addition, whilst chemical reactivity is typically interpreted to mean stability *versus* instability, it also gives an important indicator of the potential for bond activation in catalytic reactions. The majority of clusters discussed in this review are 'naked' metal particles, in the sense that they lack any organic substituents (although the chemistry of clusters with some organic shielding have also been developed in the past decade[15,20,36]), and so they typically show an intrinsic tendency to interact with other chemicals. The typically high anionic charges inhibit spontaneous agglomeration and/or the formation of metallic solids, but they also leave the cluster susceptible to electrophilic attack. The systematic exploration of the applications of Zintl clusters in bond activation reactions is thus one of the most significant recent developments in this field.[26–31]

In contrast to molecules containing (mainly) non-metal atoms where 2-centre–2-electron (2c–2e) bonding dominates (aliphatic and non-aromatic carbon compounds, for example), the increasingly inert nature of the n*s* electrons in the heavier (semi)metal atoms in Zintl clusters tends to favour electron delocalization and multi-centre-bonding.[83,84] While the finite size of known Zintl clusters (<50 atoms) prevents them from becoming truly metallic on a molecular scale, the typically intense colours (red to brownish black) of salts with sequestrated cations point to narrow HOMO–LUMO gaps. This small band gap can lead to applications in (photo)catalysis, and also makes Zintl clusters precursors of novel nanostructured or doped metals and intermetallic phases.[24,25] This list of potential applications is far from exhaustive, but it highlights the point that the motivation for developing a deeper understanding of electronic structures and bonding goes far beyond the simple interest in novel (semi)metal nano-architectures.

2.4 Theoretical methods for the treatment of endohedral Zintl clusters

Geometric structure. Before discussing electronic properties and their relationship to the available structural data, it is useful to reflect on the current position in computational cluster chemistry. As outlined in previous sections, Zintl clusters are ionic species consisting of (semi)metal elements of period 3 and below. The presence of multiple metal atoms, often from the lower regions of the periodic table, demands careful attention to a number of technical questions: (1) the choice of the appropriate quantum chemical method, (2) the treatment of relativistic effects, (3) the modelling of counter ions. The past three decades have seen the rise of density functional theory (DFT)[85] as the tool of choice in the majority of electronic structure studies on clusters. Other approaches (primarily complete active space self-consistent field, CASSCF, and its variants)[86] are just beginning to be applied to clusters, but there is no doubt that DFT remains the dominant force. The appeal of DFT is beyond question: it offers a robust tool for computing total energies and gradients at low cost, and hence provides a facile route to locate stationary points. In this way it has become possible and indeed now routine to conduct exhaustive surveys of the potential surface for any cluster composition of interest, using increasing sophisticated algorithms to identify local and global minima. It is important to emphasise, however, that DFT is not a panacea, and there is a vast array of functionals available which capture subtle (and sometimes not so subtle) differences in the relationship between the electron density and the energy. Amongst this 'functional zoo', the selection of one well-established and economically fitted representative generalized gradient approximation (GGA) functional like BP86[87,88] or PBE[89] and one representative hybrid GGA functional like B3-LYP[90] or PBE0[91] will typically span the extremes of possible outcomes ('outcome' here usually means the geometry and/or spin state of the cluster). Meta-GGA functionals like TPSS[92] or its hybrid-variant TPSSh[93] often yield a slightly better agreement with experimental data, but the improvements are usually smaller than those arising from the description of the (cationic) environment and/or from relativistic effects, which need to be considered, at least for the elements of the 5th and 6th period.[94] For the treatment of relativistic effects, a number of well-tested tools are available: effective core potentials (ECPs) fitted to fully relativistic calculations that model the inner electrons,[95] or (one-electron) exact treatments (X2C),[96] which are particularly helpful if one is interested in properties that depend on the inner electrons.[97,98] Modelling the effects of the Madelung potential generated by the counterions is essential for negatively charged clusters because otherwise the highest occupied electrons will typically be unbound (*i.e.* have positive eigenvalues). This could be achieved by using a fully periodic model, or by introducing point charges at the positions of the nearest-neighbour cations in a finite cluster model. A pragmatic alternative is the employment of the conductor-like screening model, COSMO,[99] (or the closely related polarizable embedding model, PCM), where screening charges are obtained from the boundary condition of a vanishing electrostatic potential at a shell around the cluster. As the purpose here is to mimic the effects of the Madelung potential in an approximate way, the precise choice of dielectric constant is not critical: it is common to use relatively high values; a convenient choice is that of water, but a value of infinity has been proposed by some authors.

Electronic structure. In addition to calculated energies and optimized geometries, DFT provides access to an accurate electron density and also to the wavefunction (within the Kohn–Sham construct), which in turn brings into play an array of sophisticated post-analysis tools that can be used to establish and interrogate qualitative bonding models. The invariance of the density to unitary transformations of the Kohn–Sham orbitals also provides several different orbital localization schemes that have contributed much to our

understanding of bonding. The localization of orbitals provides an intimate connection to the traditional chemist's view of a molecule in terms of lines drawn in a Lewis diagram, in a way that the canonical orbitals that reflect the full symmetry of the molecule do not. Complementary insight comes from the computation of electric and magnetic response properties, the latter providing a connection to the important concept of 'spherical (3-dimensional) aromaticity',[100] the direct analogue of Kekulé's 2-dimensional model for benzene.[101] 'Spherical aromaticity' is synonymous with the idea of non-localizable multi-centre bonding in the case of deltahedral clusters, by analogy to non-localizable double-bonds in planar aromatic molecules (see below).

3. Concepts for the description of bonding in (multi)metallic clusters: how should we look at a cluster?

The preceding paragraphs have highlighted just some of the methodological choices that are available to the computational chemist when performing calculations on Zintl ions or indeed any other class of molecules. It is tempting, then, to see the identification of the minima (and in some cases the connecting transition states) as a goal in itself, and, all too often, the end point of the study. The longevity of the work of Longuet–Higgins, Wade, Mingos and others from the pre-DFT era[58–67,69] shows us very clearly that the characterization of the structural minima should only be the starting point, from which we should seek to build an over-arching and qualitative model that unifies the properties of the clusters of interest. Ideally, one might hope to establish a single model that could encompass all clusters, but, more realistically, our present state of understanding allows only for the slightly less ambitious goal of bringing some semblance of order to different sub-families of closely related clusters, much as Wade did for the boranes almost half a century ago. Establishing links between the different families should, in the fullness of time, allow for a truly unifying model to emerge. The emphasis is therefore placed squarely on trends and patterns rather than on isolated results.

As we have noted above, the choice of model used to describe the bonding in any particular context depends strongly on the field of expertise of the scientists involved, and very different approaches have evolved amongst the chemistry and physics communities as well as between different subsections of those two disciplines. To a certain degree these differences are only a matter of the scientific language, and the alternative perspectives reflect different views of the same underlying reality. One of the main goals of this review article is thus to cut through this diversity and to identify the unifying concepts that go beyond methodological preferences. A second goal is to show how clusters and concepts that appear, at first glance, to be very diverse, are in fact more congruent than might previously have been anticipated. A case in point is the close similarity between 'empty' and endohedrally filled clusters: the metal at the centre can be viewed as a source of additional electrons and also a spherically symmetric electrostatic potential, but the fundamental electronic requirements defined by the structure of the cluster shell remain unchanged.

3.1 Cluster orbitals and localized orbitals

At the most fundamental level, molecular orbitals (MOs) are the (approximate) solutions of the Schrödinger equation for molecules. Their energies are the eigenvalues which can be interpreted as ionization energies, at least in first order (Koopmans' theorem[102]). For fundamental quantum mechanical reasons the corresponding eigenfunctions must transform according to the irreducible representations of the molecular point group, and in that sense they are necessarily delocalized. For spherical objects, the angular part of the wavefunction is identical to that for atoms, and for this reason, clusters that are approximately spherical generate MOs that resemble the atomic s, p, d, *etc.* orbitals. It is this analogy that gives rise to the term 'superatom'. It is an obvious point that no molecule is truly spherical, so the interpretative power of the superatom approach depends very much on the extent to which the (necessarily) non-spherical arrangement of the nuclei perturbs the electron density distribution. It must also be stressed that approximate sphericality is a purely geometric phenomenon, and no conclusions concerning electron delocalization or aromaticity can or should be drawn from the simple observation that canonical orbitals with the same nodal structure as atomic s, p or d orbitals emerge! As an extreme case, one may consider an (approximately) spherical arrangement of a large number of (almost) non-interacting helium atoms, where the solution of the Schrödinger equation yields MOs that are linear combinations of the 1s atomic orbitals with the same nodal characteristics as atomic orbitals, purely for symmetry reasons. Nevertheless, the electronic density of such a system differs markedly from an equally spherical cluster of alkali or alkaline earth metal atoms, to which the 'superatomic' label is typically attached. In these alkali metal clusters, the relatively weak potential due to the ionic cores can be replaced by a uniform, positively charged background without significantly changing the electronic structure of the valence orbitals. This idea is the foundation of the so-called jellium model,[73–75] which leads to energetically separated shells of cluster orbitals, and, ultimately, to the so-called 'magic' electron counts which correspond to electronic shell closures. For the He cluster, in contrast, all occupied shells of cluster orbitals are approximately energetically degenerate because the He atoms interact only very weakly.

The difference between these two limiting cases (He and Na clusters) becomes evident when we attempt to localize the canonical orbitals which, as noted above, must reflect the point group symmetry of the cluster. Common localization procedures involve a unitary transformation of the MOs to obtain an alternative set of orbitals (localized orbitals, LMOs) which are individually localized on the smallest number of atoms possible. Popular criteria for the determination of these transformations have been proposed by Boys,[103] Pipek and Mezey,[104] and others. All such processes involve the minimisation of a particular physical quantity, and so absolutely perfect localization is, in

principle, never possible: a small fraction of the electron density of each localized orbital is always located elsewhere in the molecule. Further, in contrast to the canonical orbitals, whose energies are eigenvalues that can be associated with ionization energies, the energies of localized orbitals are expectation values (a weighted average of eigenvalues) which cannot be measured, even in principle. Of course, there are technical alternatives to the 'localize and search for multi-centre orbitals' procedure: lone pairs and two-centre bonds may also be identified with Weinhold's natural bond orbital (NBO) analysis,[105] and the residual density can then be identified by subtracting the lone pairs and bonds from the total density matrix. Boldyrev and coworkers[106] have developed the AdNDP methodology, an extension of NBO for multicenter contributions, which presently requires a preceding NBO run from the Gaussian program suite. Results are usually qualitatively similar to Boys and Pipek–Mezey localization procedures (which are implemented in popular commercial and open access software). The extent to which orbitals can or cannot be localized into 1- and 2-centre components, in the entire system or in parts of it, is a very useful tool in categorizing cluster electronic structure. To come back to our example: in the He_n case, localization will restore a set of n well-localized, doubly occupied, 1s orbitals on the He atoms, while for an alkali metal cluster it will generate molecular orbitals that remain extensively delocalized over multiple centres.

In Zintl cluster chemistry, the completely delocalised and completely localized limits represent extremes of behaviour that are, in reality, never realised. However, the two extreme classes of clusters mentioned in the introductory section (electron-rich and electron-deficient) can be related directly to the concept of localizability: in a truly electron-precise situation a localization procedure will yield only 2c–2e bonds and lone pairs. Hund's localization condition[107] must be fulfilled in these cases: for each atom, the number of electrons involved in bonding must be equal to the number of nearest neighbours, and also to the number of valence atomic orbitals involved in the bonding. These requirements lead to the formation of 8 – N bonds per atom where N is the number of valence electrons (not to be confused with n, which is used throughout this article to identify the number of vertices of a cluster). For an approximately spherical cluster with n vertices this corresponds to a total requirement of $5n$ valence electrons, where n is the number of vertices, as is found, for example, in tetrahedral clusters of the group 15 element atoms such as P_4. For each atom, the lone pairs (localized on a single atom) carry the majority of the atomic s-orbital character while the p orbital character is localized primarily in the bonds to the three neighbouring atoms. The requirement to form precisely three bonds per p-block atom, and hence the total valence electron count of $5n$, is a natural consequence of the fact that for a tetrahedral main group atom, a maximum of three hybrid orbitals are directed into the same hemisphere (Scheme 2).

Clusters like Sn_9^{4-} or octahedral/icosahedral clusters, which contain hypercoordinated atoms that are connected to four or five neighbours in addition to their lone pair, do not conform to the $8 - N$ rule. Consequently, they can only be described in terms of multi-centre bonding, and localization procedures will always yield multi-centre contributions in addition to, or instead of, orbitals localized on one or two centres. Here, the Wade-Mingos rules provide a robust connection between the total electron count and the shape of the cluster.

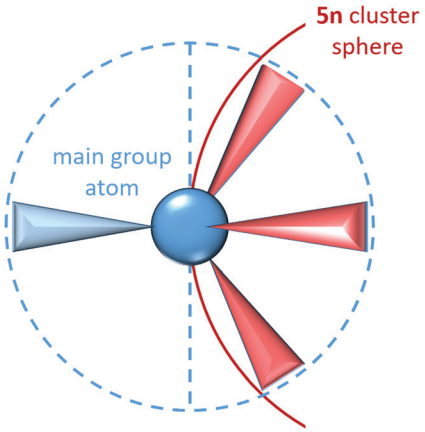

Scheme 2 Schematic representation of the bonding geometry around any main group atom incorporated in the shell of a cluster with $5n$ electrons. The blue circle and the dotted line serve to illustrate the hemisphere including three bonds (light red) that contribute to the cluster architecture, the shell of which is indicated by the red circle, while the fourth electron pair (light blue), representing a lone pair or a corresponding bond to a substituent, is directed into the other hemisphere.

Matters becomes somewhat less clear for clusters with endohedral d-block or f-block atoms: should their valence electrons be included in the total electron count or not? As we discuss in more details below, the role of the d/f electrons on the endohedral metal is a critical issue that can play a decisive role in the structural chemistry of the cluster. In a fully ionic description, the central atom can transfer all of its valence electrons to the cluster shell, allowing the latter to reach an electron-precise count. In reality, the transfer of electrons is not complete and so the LMOs representing two-centre bonds between atoms in the cluster shell usually also have small delocalization tails onto the endohedral atom. In such circumstances, whether the orbitals are regarded as 2-, 3- or multi-centred depends to a large extent on the chosen threshold for localisation.

3.2 Ring currents and the link to aromaticity

The majority of the systems discussed in this review are in some sense approximately 'spherical', and the nodal structure of the canonical orbitals resembles that of atomic orbitals: in this sense they could be considered to be 'superatomic'. However, as we have noted above, important qualitative differences become evident when we attempt to apply localization procedures in the contrasting cases of He_n and Na_n clusters. The presence of non-localizable molecular orbitals is a necessary precondition for (significant) magnetically induced ring currents, the intensity of which can be calculated from the magnetically perturbed electron density (available in most quantum chemical codes for the calculation of NMR shifts) by applying the Biot–Savart law.

The gauge-including magnetically induced currents (GIMIC) program, for example,[108] computes the total ring current by integration of the current density over a plane perpendicular to the bond axis of interest. Currents for electron-precise systems such as He_n are close to zero, while those in systems with non-localizable MOs such as Na_n can be even larger than those in benzene, the prototype for a 2-dimensional aromatic ring system. This analogy has led to a set of criteria[109] for classifying 3-dimensional molecules as aromatic (the existence of a diatropic ring current), anti-aromatic (a paratropic ring current) or non-aromatic (no significant ring current), which complement other measures such as resonance energies and equalization of bond lengths. The label '3-dimensional aromaticity' has been coined to reflect the magnetic response properties in cluster structures exhibiting multi centre bonding, typically those which are well described by the Wade–Mingos rules. However, is should be noted that, the term aromaticity is reserved for the subset of cases where at least some of the canonical orbitals are not localizable so that the electrons produce a ring current. The term does not apply *a priori* to all cases where the canonical orbitals show the nodal characteristics of spherical symmetry.

The so-called nucleus independent chemical shifts (NICS)[110] offer a single parameter to measure the magnetic response at a particular point in space, and therefore 'aromaticity' in the sense defined above. This can be done by placing one or more (dummy) atoms (*i.e.*, nuclei without nuclear charge) at the desired position, typically, a high-symmetry point where no atom is present. Both ring currents and NICS make use of the magnetically perturbed density, but the application of Biot–Savart's law for ring currents is replaced by the derivative with respect to the magnetic moment of the dummy atom in the case of NICS. It is important to bear in mind that, in contrast to ring currents, NICS are not measurable quantities, but they have nevertheless been used widely in the field of cluster chemistry. A classic example of the application of NICS come from the *closo* boranes $[B_nH_n]^{2-}$, n = 5–16, all of which have large negative (diatropic) NICS values at the geometric centre of the cluster. However, the most symmetric of these clusters, $[B_6H_6]^{2-}$ and $[B_{12}H_{12}]^{2-}$, stand out from their neighbours as the most aromatic by this measure. The applications of NICS data, together with the AdNDP methodology, in Zintl cluster chemistry has been reviewed in the recent literature.[111] In the context of endohedral clusters, however, the use of NICS calculations is limited by the presence of an atom at the cluster centre. In contrast, calculation of ring currents remains possible even in in the presence of such an atom, although care must be taken in choosing integration boundaries to exclude the contribution of the central atom to the current.

4. The correlation of electron count with structural features and further properties of multi-metallic Zintl clusters

Having established the tools and paradigms that one might apply to understand the properties of Zintl clusters, we dedicate the remainder of this review to a discussion of examples that illustrate classical bonding paradigms (specifically, electron-precise and electron-deficient clusters). We will then attempt to establish links between the two paradigms, such that all clusters can be understood within a single continuous framework that is closely connected to the total valence electron count of the cluster shell. In the following sections we will illustrate these points using selected examples from the family of known metal clusters in general and multi-metallic Zintl clusters in particular. Throughout our discussion, we will use clusters or molecules without interstitial atoms as a reference point to the description of their endohedrally 'filled' analogues. In so doing, we emphasize the role of the endohedral atom as a stabilising template and, particularly towards the left of the periodic table, its ability to contribute to the total electron budget of the p-block atom shell encompassing it. We will also highlight a number of recent examples that appear to fall between the traditional classifications – we argue that the existence of these intermediate cases reflects the changing nature of the d/f orbitals on the central metal, from diffuse and high-lying in the electron poor transition metals to core-like (in both a spatial and energetic sense) in lanthanide and actinide atoms and towards the right of the transition series. It is not our intention to give an exhaustive coverage of all known clusters – this has been done in several excellent recent reviews. Rather it is our intention to highlight cases that establish different bonding paradigms, and also those that challenge them. We will draw most but by no means all of our examples from the family of 12-vertex clusters because this offers the most diversity, in terms of both composition and structure – and also because the 'metalla-plumbaspherene', $[Pt@Pb_{12}]^{2-}$, is an iconic example of an isolable endohedral Zintl cluster, reported for the first time by Eichhorn in 2004.[53]

An overview of the ground to be covered is shown in Scheme 3. The horizontal axis defines the number of cluster vertices and, as noted above, our choice to emphasise the 12-vertex family reflects the great diversity to be found there. The vertical axis defines the valence electron count, ranging from highly electron-deficient (hypoelectronic) clusters with ***4n*** valence electrons at the bottom to electron-precise crown-like clusters with ***6n*** valence electrons at the top. This series, spanning 24 electrons in the 12-vertex family, captures the transition from highly delocalised multi-centre bonding at the bottom to localized 2c–2e bonding at the top. The 2-dimensional perspective reflects the diversity of models used to understand the relationship between structure and bonding: relationships between clusters with the same electron count but different number of vertices (diagonal relationships in the scheme), *versus* the development of the structures from deltahedra towards three-bonded polyhedra, and finally, crown-like structures on changing electron count within a fixed vertex count (vertical relationships in the scheme). Note that we focus on clusters with exclusively p-block (semi)metal shells, and, wherever applicable, we draw parallels between 'empty' clusters or other

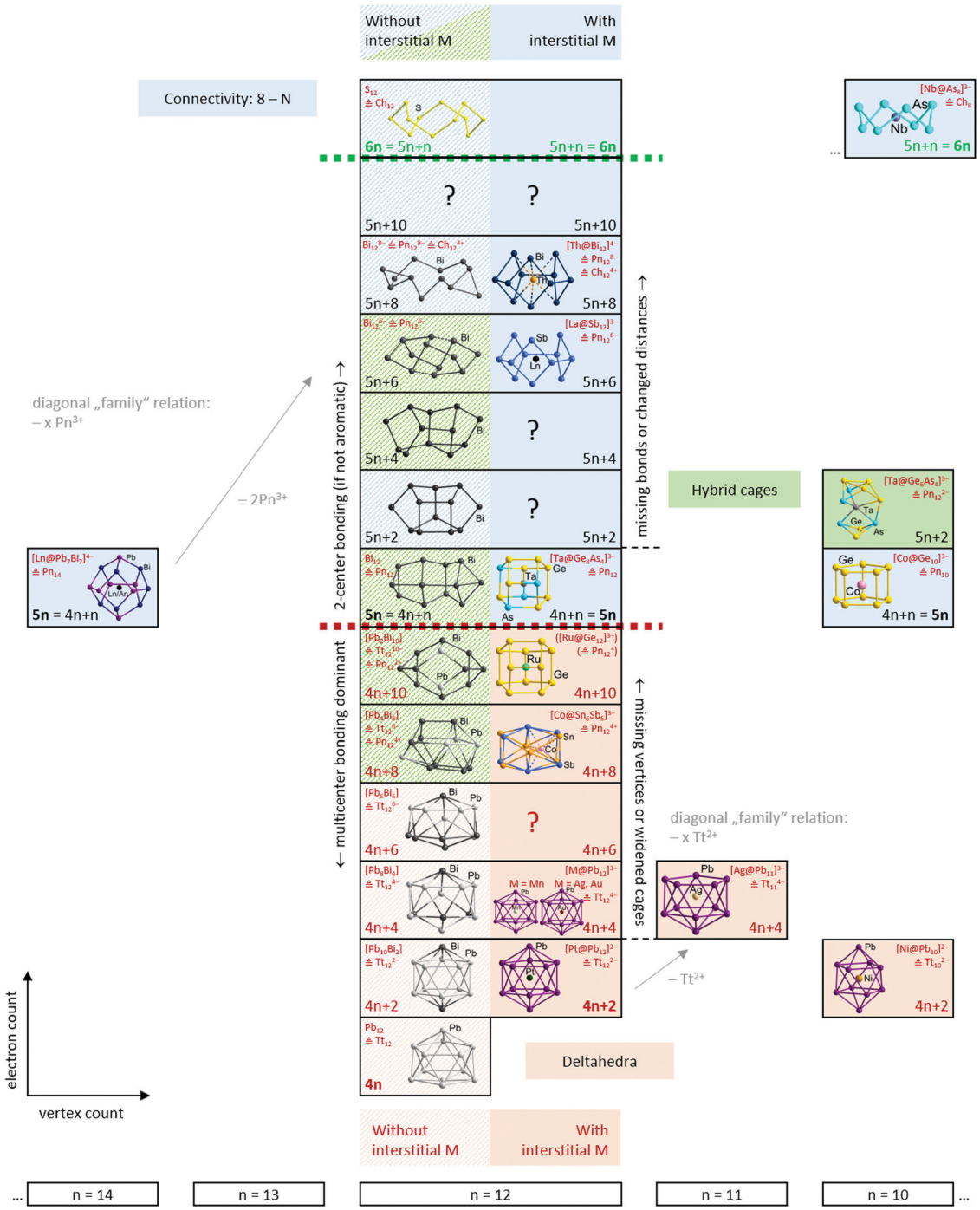

Scheme 3 The structural development of clusters with **4*n*** to **6*n*** valence electrons, illustrated for the cluster family with 12-vertex atoms as an example. Cluster species that have an experimental precedence from X-ray diffraction are drawn in colour, species which are known only from DFT calculations are drawn in grey-shade. Electron/vertex counts that have not yet been reported in any experimental or theoretical study are indicated by a question mark. Examples for clusters that belong to adjacent families and show a close structural relationship are added to the left and to the right where applicable. References to the clusters shown and enlarged illustrations of their structures to be found in the text.

well-known molecules on the one hand and endohedral clusters on the other.

4.1 Electron-precise endohedral Zintl clusters: from 5*n* to 6*n*

'Empty' clusters. Electron-precise clusters provide a natural reference point for a wider description of electronic structure simply because it is possible to localise all of the available valence electrons into single-centre lone pairs or 2c–2e bonds. The corresponding total valence electron count is at least **5*n*** (where *n* is the number of vertices), of which **2*n*** constitute lone pairs (Lp) (or *exo*-bonding pairs for ligand binding) directed radially outwards from the cluster, with the remaining $\geq$**3*n***

electrons participating in bonding pairs (B). The numbers of lone- and bonding pairs can be calculated according to the following succinct expressions: B = $4n - t/2$ and Lp = $t - 4n$ (t: total electron count, n: number of (non-hydrogen) atoms).[66,68]

We will illustrate the general concept for classical 'empty' examples first, before progressing to endohedral Zintl clusters that can also be considered as electron-precise. As a result of the division of the electron reservoir into $2n$ electrons for lone pairs (or exo bonds) and the remainder for cluster bonding, the natural structural preference is for each vertex to be bonded to precisely $8 - N$ others as observed in tetrahedral P_4 or As_4 ($N = 5$) or cyclic S_8 ($N = 6$). The isoelectronic tetrahedral Tt_4^{4-} anions Si_4^{4-}, Ge_4^{4-}, Sn_4^{4-} and Pb_4^{4-} are all known in Zintl phases or Zintl salts[112] and also in discrete coordination compounds such as $[Zn_6(Ge_4)_4]^{4-}$ [113] and $[Au(Sn_4)_2]^{7-}$.[114] Several binary P_4 analogues have also been reported as Zintl salts of anions $(TrBi_3)^{2-}$ (Tr = Ga, In Tl), $(Tt_2Pn_2)^{2-}$ (Tt/Pn = Ge/P, Ge/As, Sn/Sb, Sn/Bi, Pb/Sb, Pb/Bi).[115–122] Coordination compounds of some of them, $(Ge_2As_2)^{2-}$, $(Sn_2Sb_2)^{2-}$, or *in situ*-generated $(Ge_3P)^{3-}$ and $(Ge_3As)^{3-}$, have also appeared in the recent literature:[122–124] the gold cluster $[Au_6(Ge_3As)(Ge_2As_2)_3]^{3-}$,[124] for example, is precisely isoelectronic with the aforementioned homonuclear $[Zn_6(Ge_4)_4]^{4-}$. The reduced anionic charge in the heteroatomic group 14/15 clusters confers significant advantages in terms of both stability and solubility, and these binary P_4 analogues show great promise as synthons for the growth of larger, multinary clusters.[19,21,36,121] One drawback, however, is that the characterisation of multi-metallic, as opposed to homo-nuclear, cluster units, is complicated by the difficulties associated with differentiating elements with similar atomic numbers using X-ray diffraction. In such circumstances, careful computational surveys of the potential energy surfaces have allowed the favoured positions of atoms that are neighbours in the periodic table to be established.[125,126] The (pseudo-)tetrahedral units represent the only non-endohedral inorganic clusters that contain exactly $5n$ electrons; to find larger isolated examples, we have to move to the gas-phase or consider inherently unstable species such as prismane (C_6H_6, an isomer of benzene) and cubane (C_8H_8, an isomer of cyclooctatetraene). The stability of larger homo-nuclear analogues of the group 14 clusters is likely to be compromised severely by the ever higher negative charges required to attain the $5n$ electron count. This problem can, however, be mitigated to some extent by the incorporation of both group 14 and 15 elements in the same cluster, which lowers the charge (as described above for the Tt_4^{4-} series and their binary analogues $(Tt_2Pn_2)^{2-}$) or of endohedral atoms or ions that can contribute to the total electron count. Another strategy for lowering the overall charge on a cluster of group 14 element clusters with an electron count of $5n$ or more is to bind external counterions closely, for example in the formation of the 16-vertex Frank–Kasper polyhedron $(Li_4Ge_{12})^{8-}$.[127] The presence of four Li^+ cations intimately bound to the Ge_{12}^{12-} cage stabilises what would otherwise be a very unstable three-connected $5n$-electron cluster (Fig. 2).

In clusters with a $5n$ electron count, the canonical molecular orbitals typically show large HOMO–LUMO gaps. Localization algorithms then readily partition the density into lone pairs and orbitals localized over 2 centres, in accordance with the expectation of 2c–2e bonding in electron-precise clusters. For clusters where the electron count exceeds $5n$, the additional electrons are accommodated in antibonding canonical orbitals, with the consequence that one or more bond is broken. In a localized ansatz, the combination of a bonding orbital and its antibonding counterpart that are both occupied generates lone pairs on two centres. From either perspective, clusters with more than $5n$ electrons are expected to adopt less symmetric structures with a mixture of 3-connected and 2-connected vertices.

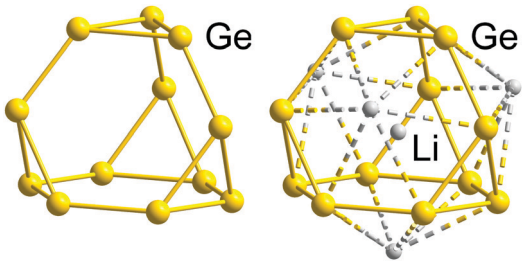

Fig. 2 Molecular structure of the electron-precise Ge_{12}^{12-} skeleton (left), with 60 = $5n$ electrons found in the structure of the ternary alloy $RbLi_7Ge_8$, and that of the actual cluster stabilised by four outer and one inner Li^+ cations in this phase, $[Li^+@(Li_4Ge_{12})^{8-}]^{7-}$ (right), exhibiting a Frank–Kasper-type 16-vertex polyhedron with 64 = $4n$ electrons.[127]

A simple example of a more electron-rich cluster (with $5n$ + 2 = 22 electrons) is the butterfly-shaped Si_4^{6-} anion found in Ba_3Si_4, where one of the six bonds of the Si_4^{4-} tetrahedron has been broken, while two lone pairs are created at the respective Si atoms. This cluster and the isoelectronic borane B_4H_{10} also highlight some of the ambiguities that emerge when considering different electron-counting schemes. The B_4H_{10} cluster would conventionally be viewed as an *arachno* cluster in the Wade-Mingos terminology, with a characteristic total valence electron count of $4n + 6$. Of course for $n = 4$, $4n + 6 = 5n + 2$, and these clusters are rare examples where the structure can be understood from both perspectives, either as an 'electron-precise' or an 'electron-deficient' (*arachno*-type) cluster. As illustrated in Scheme 4, similar coincidences occur for $n = 3$ ($6n = 4n + 6 = 18$), $n = 4$ ($5n = 4n + 4 = 20$ and $5n + 2 = 4n + 6 = 22$) and for $n = 6$ ($5n = 4n + 6 = 30$). In a similar vein, we can connect the apparently rather disparate triad of C_8H_8 (as the gyrobifastigium-type[131] cuneane isomer), S_4N_4, S_8^{2+} and S_8 by noting that their respective electron counts are 40 (= $5n$), 44 (= $5n + 4$), 46 (= $5n + 6$), and 48 (= $5n + 8 = 6n$ for $n = 8$), so they have 12, 10, 9 and 8 bonding pairs, respectively.

Polyphosphide chemistry also provides us with many prominent examples of clusters possessing $5n + x$ electrons, for instance, the nor-tricyclane-type P_7^{3-} and the 'ufosane'-type P_{11}^{3-} clusters. All heavier homologues of both Pn_x^{3-} anions with Pn = As, Sb, Bi are also well established.[132,133] In these clusters, the neutral Pn atoms, with 5 valence electrons have $8 - N = 3$ nearest neighbours and one lone pair (as for P_4 above), while the three negatively charged Pn^- centres (isoelectronic with S) have 6 valence electrons and consequently form only $8 - N = 2$ bonds, along with two lone pairs. Charged

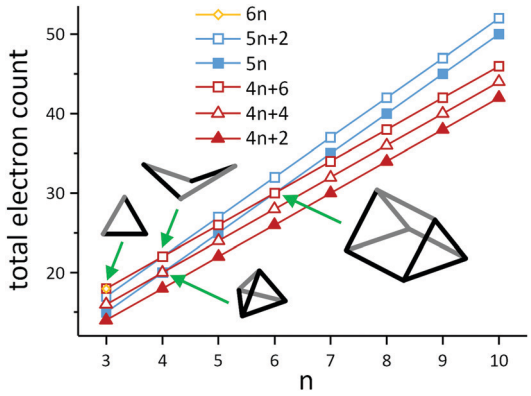

Scheme 4 Illustration of the development of total electron counts in electron-deficient clusters with **4*n*** + **2** (*closo*-type), **4*n*** + **4** (*nido*-type) and **4*n*** + **6** (*arachno*-type) electrons on the one hand (red) and electron-precise clusters with **5*n*** or **5n** + **2** electrons (blue) or **6*n*** electrons (yellow) on the other hand. Note that the lines only serve as a guide to the eye. The structural diagrams represent the four types of clusters, in which the families overlap. The triangle (n = 3) lies at the intersection of **6*n*** = 18 and **4*n*** + **6** = 18 electrons, hence it can be viewed as an electron-precise cluster or an *arachno*-type cluster (trigonal bipyramid minus two vertices; example: Pn_3^{3-} (Pn = Sb, Bi);[128,129] the butterfly structures (n = 4) can be either understood as an electron-precise cluster with **5*n*** + **2** = 22 electrons or as an *arachno*-type cluster with **4*n*** + **2** = 22 electrons (octahedron minus two vertices; example: Si_4^{6-}); a trigonal pyramid (n = 4) corresponds either to an electron-precise cluster with **5*n*** = 20 electrons or to a *nido*-type cluster with **4*n*** + **4** = 20 electrons (trigonal pyramid minus one vertex; example: Sn_4^{4-}); the trigonal prism (n = 6) can be described as either an electron-precise cluster with **5*n*** = 30 electrons or an *arachno*-type cluster with **4*n*** + **6** = 30 electrons (trigonal dodecahedron minus two vertices; example: Te_6^{6+}).[130]

centres can be considered as pseudo-atoms of the neighbouring group in the periodic table, which, in the case of P_7^{3-}, highlights the structural correspondence with P_4S_3 and P_4Se_3. For P_4S_3, for example, the total number of valence electrons is 38, with 4·7 − 19 = 9 bonding pairs and 38 − 4·7 = 10 lone pairs. In principle, all isoelectronic systems should behave in this way, although the absolute structures cannot be predicted *a priori*, particularly for larger systems where more than one isomer may satisfy the equations for B and Lp indicated above. The ufosane-type P_{11}^{3-} anion represents the largest known 'spherical' Zintl-ion cluster in the electron-precise category; beyond this size, catenation of distinct cluster units is the dominant growth pattern rather than further expansion into larger, still approximately spherical, clusters. Examples include larger polyphosphides or -arsenides and binary anions like $(Ga_4Bi_{14})^{4-}$ or $(Ga_2Bi_{16})^{4-}$.[134,135]

Endohedral clusters. As outlined above, the expansion of the field to endohedral Zintl clusters by encapsulation of d-block or f-block atoms, and potentially the expansion to binary clusters which can further moderate the charge, has led to a number of quite remarkable structures in recent years. Replacement of some of the group-15 elements with group 14 analogues has led to the isolation of the 12-vertex $[Ta@Ge_8As_4]^{3-}$ and the 14-vertex $[Ta@Ge_8As_6]^{3-}$clusters.[121] Although the incorporation of group 14 elements in the cluster shell decreases its electron count relative to a purely group 15-atom clusters, the structures of the cluster shells formed in these cases remain consistent with valence electron counts of 60 and 70. From a localized perspective, the transfer of all electrons from the group 5 metal to the cluster shell converts five group 14 atoms (Ge) into pseudo-group 15 atoms (Ge^-) and as a result the D_{2d}- and D_{3h}-symmetric frameworks of $[Ta@Ge_8As_4]^{3-}$ and $[Ta@Ge_8As_6]^{3-}$ feature the exclusively 3-connected vertices that are the structural signature of a **5*n*** electron count (Fig. 3). Note that the precise positions of the Ge and As atoms (Z = 32 and 33, respectively) are again difficult to ascertain from the X-ray data alone, and a precise structural assignment relies on complementary DFT calculations. A closely-related example with a homonuclear shell comes in the form of the $[Ru@Ge_{12}]^{3-}$ anion, with rigorous D_{2d} point symmetry (Fig. 4).[136] The valence electron count in $[Ru@Ge_{12}]^{3-}$ is 59 (= **5*n*** − **1**) rather than 60, and a detailed analysis of the electron structure shows that the single vacancy in the valence manifold is located in an orbital of a_2 symmetry localised exclusively on the Ge_{12} cage Moreover, this orbital also has no Ge 4s character on 4 of the 12 vertices, leading to a highly diagnostic hyperfine coupling pattern to only 8 of the 12 Ge nuclei in the EPR spectrum.

Finally, we note that whilst our emphasis has been on 12-vertex clusters, 3-connected architectures have also been identified in smaller clusters of germanium, notably pentagonal prismatic (D_{5h}) $[Fe@Ge_{10}]^{3-}$ and $[Co@Ge_{10}]^{3-}$ [137,138] with total valence electron counts of 51 and 52, respectively, compared to a **5*n*** count of 50. In this case, however, the excess electrons (1 and 2, respectively) are localised in a metal d_{z^2} orbital which is non-bonding with respect to the 50-electron cage. Therefore, these clusters are considered to be electron-precise, too, in agreement

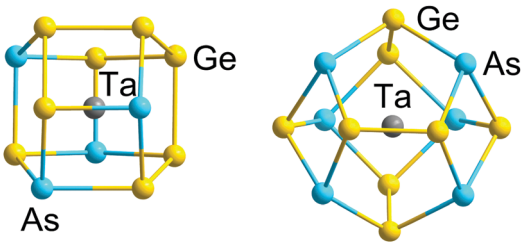

Fig. 3 Structures of 12-vertex and 14-vertex clusters $[Ta@Ge_8As_4]^{3-}$ (left) and $[Ta@Ge_8As_6]^{3-}$ (right) with **5*n*** valence electrons (60 or 70) in their binary cluster shells.[121]

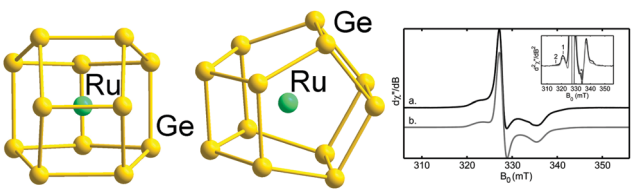

Fig. 4 Structure of the binary cluster $[Ru@Ge_{12}]^{3-}$ with 59 (**5*n*** − **1**) valence electrons (left and centre, two views), and the measured and simulated EPR signals indicating the radical character (right). The graphic on the right hand side has been reproduced from ref. 136 with permission from ACS, copyright 2014.

with a three-bonded nature of the Ge atoms (with somewhat longer distances between the two pentagonal Ge_5 faces, 2.608 Å on average, than within the faces, 2.517 Å on average). The significant contribution of Co(3d) orbitals to the bonding MOs is elegantly illustrated in real-space by the electron localization function (ELF) shown in Fig. 5.[139]

An even more electron-rich situation is found in endohedral clusters of the type $[Ln@Sb_{12}]^{3-}$ (Ln = Y, La, Ho, Er, Lu),[140] which formally contain an Ln^{3+} ion at their geometric centre, encapsulated by a doughnut-shaped 66-electron Sb_{12}^{6-} anion based on three linked 4-membered rings. The electron count sits precisely midway between **5*n*** and **6*n*** (thus, **5*n* + 6**), and the resultant combination of 2- and 3-connected vertices (6 of each type) in the doughnut-type p-block atom shell is fully consistent with the $8 - N$ rule, and all available electrons can again be localized in 2c–2e bonds (Fig. 6). Notably, the electrostatic stabilisation by a central metal ion is crucial here, which becomes obvious when comparing the structure with that of (hypothetical) 'Bi_{12}^{6-}' anion (see Scheme 3), where the absence of a metal centre leads to a more oblate geometry.

A further 2 or 3 additional valence electrons are accommodated in the related clusters $[Th@Bi_{12}]^{4-}$ (Fig. 7) and $[U@Bi_{12}]^{3-}$.[83,141] As for the lanthanide-centred analogues, the endohedral atoms favour 3-dimensional structures which minimise the distance between the metal cation and the formally anionic (2-bonded) Bi^- vertices. The first two additional electrons fill the LUMO of 'Bi_{12}^{6-}', which then becomes the HOMO for the 'Bi_{12}^{8-}' unit, and the third additional electron in the uranium cluster enters a 5f orbital. The HOMO for $[Th@Bi_{12}]^{4-}$ displayed in Fig. 7 shows extensive π-delocalization and, in contrast to all other molecular orbitals, is inherently not localizable. For these 2π-systems, quantum chemical studies indicate the presence of remarkably strong ring currents,

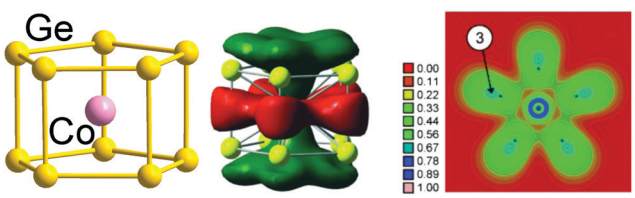

Fig. 5 Structure (left), one of the bonding MOs (centre) and plot of the electron delocalization function (ELF; right). The figure has been adopted from ref. 138 with permission from Wiley VCH, copyright 2009.

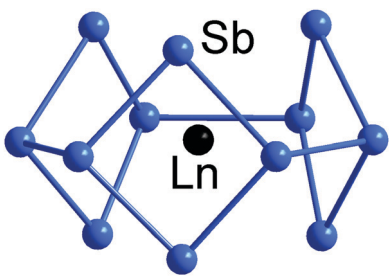

Fig. 6 Structure of $[La@Sn_{12}]^{3-}$ with **5*n* + 6** = 66 valence electron in its 12-vertex shell.[140]

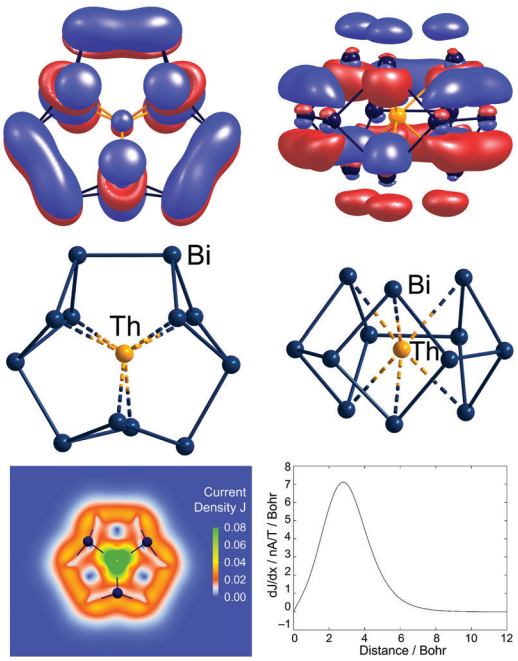

Fig. 7 The non-localisable HOMO of $[Th@Bi_{12}]^{4-}$, accommodating the additional electron pair of the total of **5*n* + 8** valence electrons (top, two views) and the structure in its 12-vertex shell (centre, two views). The inherent non-localizability of the HOMO causes a significant ring current of this 2π–aromatic cluster (bottom). This figure has been adopted from ref. 83 with permission from Springer-Nature, copyright 2021.

24.8 nA T^{-1} for $[Th@Bi_{12}]^{4-}$ (Fig. 7). This value is similar to that in 26π-aromatic porphine (25.3 nA T^{-1}), despite the much lower number of π-electrons involved. The occupation of the delocalized orbital in the actinide compounds also introduces a π component to the Bi–Bi bonds between the four-membered rings, which leads to a significantly narrower range of Bi–Bi bond lengths for these compounds (Bi–Bi = 3.04–3.13 Å for $[Th@Bi_{12}]^{4-}$) compared to the Sb–Sb bonds in $[La@Sb_{12}]^{3-}$ (2.80–3.04 Å).

This comparison highlights the close connection between aromaticity and the lack of dispersion of bond lengths. The structural contrast between these clusters and the 'empty' (and unknown) 'Bi_{12}^{8-}' anion is again striking – the absence of an endohedral metal ion causes the cluster to open out into an oblate crown-like geometry that maximises the distances between the anionic *pseudo*-group 16 Bi^- centres (see Scheme 3).

A further increase in electron count (relative to **5*n***) leads to an even greater dominance of 2-connected over 3-connected vertices. One of the limiting cases is the (idealized) D_{3d}-symmetric Sn_6^{12-} ring in $[Sn_6\{Nb(\eta^6\text{-}C_6H_5Me)\}_2]^{2-}$, although this cluster is probably best considered as an inverted sandwich-type structure rather than an interstitial cluster.[142] However, (formal) transfer of all 5 valence electrons from both Nb atoms increases the valence electron count at the polystannide crown to 36 (= **6*n***), and the arrangement of Sn atoms similar to a chair-like conformation of C_6H_{12} cyclohexane or S_6, where all electrons can be localized into lone pairs or 2e–2c bonds. One further examples where the group 5 metal donates (at least formally) all 5 of its valence electrons to the cluster electron count

is the D_{4d}-symmetric 48 (= **6*n***)-electron $[Nb@As_8]^{3-}$ anion, where all 8 vertices are bonded to 2 others in a crown, isostructural and isoelectronic to S_8.[143]

4.2 A close-up of the nature and role of the endohedral atom

The electron counts reported in the previous paragraphs have been based on the assumption that all of the transition metal d electrons contribute to the electron count at the cluster. It is, then, no coincidence that all of the transition metals involved (Nb, Ta, Ru, Fe, Co) are relatively early in the transition series, and all, with the possible exception of Fe and Co, have relatively accessible higher oxidation states. Whilst the formulation of $[La@Sb_{12}]^{3-}$ (Fig. 6) as La^{3+} and Sb_{12}^{6-} is uncontroversial, and $[Ta@Ge_8As_4]^{3-}$ (Fig. 3) as Ta^{5+} and $(Ge_8As_4)^{8-}$ is plausible in light of the known oxidation states of the elements involved, it is less realistic to think of $[Ru@Ge_{12}]^{3-}$ (Fig. 4) as containing Ru^{8+} and Ge_{12}^{11-}. Nevertheless, the covalent interactions between the cluster orbitals and the d orbitals on the metal are clearly sufficient to allow the d electron density to imprint itself on the cluster shell, forcing it to adopt a structure that, in the absence of the metal, would be characteristic of a much higher negative charge. This, then, immediately raises the question of what happens when the d electrons on the transition metal become less accessible, as they inevitably must as we move towards the right hand side of the transition series. An important illustration for this case comes from the comparison of $[Ta@Ge_8As_4]^{3-}$ (Fig. 3 left) with $[Ni@Pb_{12}]^{3-}$:[144] both would have **5*n*** = 60 valence electrons if all metal d electrons were included in the count, which amounts to the assumption that the interstitial ions adopt Ta^{5+} and Ni^{10+} oxidation states, respectively. The unrealistic nature of the latter has the consequence that $[Ni@Pb_{12}]^{2-}$, like all filled metallaspherenes, is icosahedral rather than D_{2d}-symmetric – in full agreement with the more chemically reasonable idea of the Ni atom retaining all of its valence electrons in a d^{10} shell and transferring none of them to the p-block atoms (Ni^0). The deltahedral structure, based on triangular faces, is highly characteristic of electronic-deficient clusters with **5*n* − 10** = 50 = **4*n* + 2** valence electrons (for n = 12), familiar to many readers through Wade's classic work on boranes.

4.3 Electron-deficient endohedral Zintl clusters: from 4*n* to 5*n* − 2

'Empty' clusters. It is immediately apparent from the deltahedral structures of typical *closo*-boranes such as the octahedral $[B_6H_6]^{2-}$ and icosahedral $[B_{12}H_{12}]^{2-}$ that a bonding model based on localized 2c–2e bonds cannot be appropriate: there are simply not enough electrons available to assign 2 to each line in the structural diagram! As a result, orbital localization schemes are typically much less successful in this class of cluster than in their electron-precise analogues. In such circumstances, the total electron count is a more useful quantity than the number of electrons at a particular vertex, and this is the parameter on which we focus in the following discussion.

The adoption of deltahedral structures with triangular faces is, in fact, highly characteristic of a broad class of 'electron-deficient' clusters, *i.e*, those with fewer than **5*n*** valence electrons. $[B_{12}H_{12}]^{2-}$, for example, has 50 (= **5*n* − 10** = **4*n* + 2** for n = 12) valence electrons, so is manifestly more 'electron-deficient' than $[Ta@Ge_8As_4]^{3-}$, with 60 valence electrons in the 12-vertex cluster shell. The icosahedron is a relatively common motif in Zintl-ion chemistry but Zintl-ion analogues of the smaller boranes such as $[B_6H_6]^{2-}$ are rare. One beautiful example, however, is the $[Sn_6\{Cr(CO)_5\}]^{2-}$ cluster reported by Huttner and co-workers,[145] which contains an octahedral $[Sn_6]^{2-}$ core, isolobal with $[B_6H_6]^{2-}$, with **4*n* + 2** = 26 valence electrons. The **4*n* + 2** count is generally characteristic of '*closo*' structures where the atoms sit at the vertices of a perfect deltahedron such as an octahedron or icosahedron. The 'magic' stability of the **4*n* + 2** electron count can be rationalised by noting that each vertex bears an *exo*-type B–H bond (or a lone pair in the case of Zintl-ions), accounting for **2*n*** = 12 of the electrons in the octahedral clusters and **2*n*** = 24 in an icosahedron. This then leaves **4*n* + 2 − 2*n*** = **2*n* + 2** = 14 valence electrons (the so-called skeletal electrons) to form the bonds that bind the B_6 or Sn_6 cluster units. Two of these 14 electrons occupy a totally symmetric combination of atomic orbitals directed inwards to the centre of the cluster while the remaining **2*n*** occupy a further n bonding combinations of orbitals that are oriented around the surface of the cluster, tangential to the surface norm. These n + 1 bonding (and occupied) MOs are well separated from the **2*n*** – 1 antibonding (and unoccupied) MOs, emphasising the imbalance between occupied and vacant orbitals that is characteristic of electron-deficiency. The real power of the Wade–Mingos model lies in its ability to (a) establish a conceptual connection between clusters which share the same skeletal electron count but differ in the number of vertices, and (b) allow a transfer of the electron-count/structure correlation to other isoelectronic (or isolobal) atoms or groups, and hence also to p-block atoms of any kind. As an illustration, we can highlight the progression from $[B_6H_6]^{2-}$ to C_{4v}-symmetric *nido*-B_5H_9, a square pyramidal structure with a total valence electron count of **4*n* + 4** = 24, and to the 'butterfly' structure of *arachno*-B_4H_{10}, with a total count of **4*n* + 6** = 22. In the Zintl-ion domain, we can trace the same progression from Sn_6^{2-} to the (as yet unknown) Sn_5^{4-} (24 electrons), and to the 22-electron Si_4^{6-} anion found in Ba_3Si_4. We have highlighted above the ambiguities that emerge when different paradigms intersect, as they do for B_4H_{10} and Si_4^{6-}, where the total valence electron count of 22 equals both **4*n* + 6** and **5*n* + 2**.

The structures of many Zintl clusters, both with and without endohedral metal atoms, can be understood in terms of Wade's rules, and in fact the vast majority fall into the *closo* category. Rather like the electron-precise family, empty clusters (*i.e.*, those without an endohedral metal) are common for smaller species, the smallest example being the trigonal prismatic tetrelide anions Tt_5^{2-} (Tt = Si, Ge, Sn, Pb),[146–150] and their isostructural analogues Tl_5^{7-} and Bi_5^{3+},[151–153] with total electron counts of 22 (= **4*n* + 2**). 9-Vertex *nido*-clusters such as Tt_9^{2-} (Tt = Si, Ge)[154–156] are well known, and the bicapped square antiprismatic *closo*-Pb_{10}^{2-} anion has also been isolated and unambiguously characterised crystallographically,[157] while the still elusive Ge_{10}^{2-} anion was found to coordinate an $\{Mn(CO)_4\}$ fragment in $[Ge_{10}Mn(CO)_4]^{3-}$.[158] The larger Sn_{12}^{2-} and Pb_{12}^{2-} clusters have been observed in the gas phase by Wang,[159,160] but could not be isolated in the condensed phase.

Whilst this may reflect crystallization issues for the generally robust 12-vertex clusters (according to DFT studies, see Scheme 3), it may also signal the collapse of clusters with large central cavities into more compact globular clusters. Comprehensive DFT calculations using a genetic algorithm on 'empty' 12-vertex clusters running from Pb_{12} through mixed $Pb_{12-x}Bi_x$ species (x = 1–11) to Bi_{12}, spanning electron counts of $4n$ to $5n$ valence electrons, indicated that in the absence of a central atom, cluster architectures other than the deltahedron are the global minima (see Scheme 3).[161] The only global minimum that corresponds to an experimentally known geometry is found for (hypothetical) $Pb_{10}Bi_2$, a *closo*-type structure with $4n + 2$ valence electrons. All other clusters, including the 12-vertex structure of (hypothetical) Bi_{12} with a $5n$ valence electron count, require the presence of a central atom – either for electrostatic stabilisation or covalent bonding, or a mixture of both.

For all isolated cases of electron-deficient metal clusters, the minimum number of electrons is $4n + 2$. The lower $4n$ electron count – associated with the label pre-*closo* or *hypoelectronic* – has been reported for small monovalent clusters of group 13 atoms such as the boron subchlorides, $(BCl)_n$ (n = 4, 8, 9)[162–164] the related aluminium clusters $(AlCp^*)_4$ (Cp^* = C_5Me_5), and Tl_7^{7-},[165] which actually possess *closo*-type architectures.[10–12] According to DFT calculations on 'empty' Pb_{12} the $4n$-electron species undergoes a distortion to a compressed icosahedron (see Scheme 3).[161]

Proceeding in the opposite direction, a stepwise increase of the total number of valence electrons above $4n + 2$, generates structures that resemble fragments of deltahedra, with one (*nido*), two (*arachno*), or even three vertices (*hypho*) missing relative to a (hypothetical or existing) *closo* cluster deltahedron. The descriptor '*nido*' is typically applied to clusters with a $4n + 4$ count to reflect their 'nest-like' structure while '*arachno*' captures the resemblance to a spider's web shown by the $4n + 6$ family. Generally, this pattern holds for electron deficient Zintl anions but, in contrast to the many examples of *closo* Zintl-ion clusters, analogues of the *nido*, *arachno* and *hypho* clusters that dominate the chemistry of the boranes are relatively scarce. Amongst the family of empty Zintl ions, the 9-vertex Tt_9^{4-} clusters (Tt = Si, Ge, Sn, Pb) have been studied extensively.[166] They possess $40 = 4n + 4$ valence electrons and adopt a capped square anti-prismatic geometry typical of *nido* clusters. Moreover, they are sufficiently stable to be used as a starting materials in the synthesis of larger Zintl cluster compounds. The 8-vertex $[Sn_5Sb_3]^{3-}$ has also been reported very recently, with a structure that is unknown in borane chemistry but is consistent with an *arachno* ($4n + 6 = 38$) electron count. A detailed survey of the potential energy surface for this anion reveals three distinct low-lying isomers for the 8-vertex, 38-electron cluster, all of which can be derived from the 10-vertex *closo* bicapped square antiprism *via* the loss of two vertices. The isomer observed for the binary Zintl anion is described as iso-arachno with respect to the borane analogue, highlighting an important difference between non-metal and metal clusters. The boranes comply strictly with Wade's rules, *i.e.*, they release neighbouring corners when going from *closo* to *arachno* cages in order to retain a maximum number of triangular faces for efficient multi-centre bonding. Metal clusters, in contrast, can also tolerate other forms of cluster deconstruction where mutually *trans* vertices are removed. Square antiprismatic Sn_8^{6-} (in $Rb_4Li_2Sn_8$),[167] for example, can be derived formally from an E_{10}^{2-} parent structure by removal of two opposing vertices. The higher negative charge and greater degree of electron delocalization in metal clusters, along with their ability to form intimate contacts to counterions such as Li^+, gives access to a wider range of structural alternatives.

Endohedral clusters. The encapsulation of a closed-shell (d^{10}) transition metal atom or ion into the centre of a p-block metal cage also serves to stabilise electron-deficient clusters and was in fact a key step in their isolation. Rather few examples are known for small *closo*-type cages, although $[Ni@Pb_{10}]^{2-}$ has the same bicapped square antiprismatic architecture as its empty parent, Pb_{10}^{2-}.[168] The most prominent examples are again found in the 12-vertex family. An endohedral atom placed at the centre of a Tt_{12}^{2-} 12-vertex cage stabilises the cluster without changing the electron count of the p-block (semi)metal shell, at least in the limit that the d electrons are sufficiently core-like to eliminate covalent interactions with orbitals localised on the shell. There are now very many ions of this type known, including $[M@Pb_{12}]^{2-}$ (M = Ni, Pd, Pt) and $[M@Sn_{12}]^{3-}$ (M = Rh, Ir),[169,170] and also the isoelectronic, purely p-block species $[Tl@Tl_{12}]^{11-}$,[171] all of which have the almost perfect icosahedral geometry characteristic of the $4n + 2 = 50$ skeletal electron count. The structure of $[Ir@Sn_{12}]^{3-}$ is shown in Fig. 8 as a representative of these related cluster species.

Detailed photo-electron spectroscopic (PES) measurements have been made on a number of these clusters, including the $[M@Sn_{12}]^-$ systems (M = Cu, Ni, Co, Fe, Cr, V, Tl, Au, Pt, Nb).[39] The spectra are illustrated in Fig. 9. The rather invariant orbital energies of the h_g, t_{1u}, and g_u bands, and the resemblance of the measured spectrum to the eigenvalue spectrum of the computed canonical orbitals (Fig. 10) is striking, as is the similarity between $[M@Pb_{12}]^{2-}$ and the empty Pb_{12}^{2-} cage. The latter point highlights the relatively clean separation between orbitals localized on the metal and those localized on the cage.

In comparison to both boranes and the 'empty' metal polyanions and polycations, endohedral Zintl clusters appear to show a much reduced propensity to adopt classically *nido*-type cluster structures. Instead, they prefer somewhat expanded and distorted versions of more spherical geometries that might be thought typical of a *closo* electron count. A striking example is the family of endohedral clusters, $[M@Sn_9]^{q-}$ (M/q = Co/5, Ni/4, Cu/3), studied extensively by Fässler, Sevov, Corbett and others, all of which can be formulated as $[M@Sn_9^{4-}]^{q-}$ with M being a neutral or charged d^{10} metal atom (Co^-, Rh^{2-}, Ni, Cu^+).[172–174] This work highlights the important point that the monocapped square antiprism, the classic *nido*-type structure, is very similar in energy to a tricapped trigonal prism (the structure expected for a *closo* electron count), albeit with elongated edges. Clearly, the precise structure adopted in any given case is very sensitive to the surrounding crystalline lattice as a result of rather weak metallic bonds and the soft vibrational modes that allow for small deformations. There

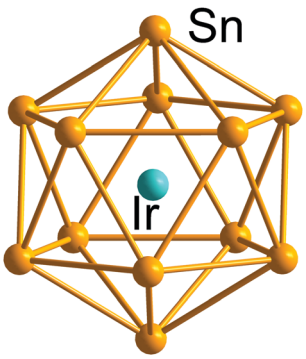

Fig. 8 Structure of the archetypical 12-vertex *closo*-type icosahedron in $[Ir@Sn_{12}]^{3-}$.[170]

are a number of possible reasons for this general preference for approximately spherical (albeit distorted) geometries over genuinely *nido* alternatives. One is that the cage is intrinsically more flexible in Zintl ions compared to boranes, due to the different characteristics of metal–metal *vs.* B–B bonding. The other relates to the nature of the interaction between the interstitial d-block or f-block atom with the p-block (semi)metal atoms of the cluster shell. The endohedral metal atom generates a spherical potential at the centre of the cluster which will

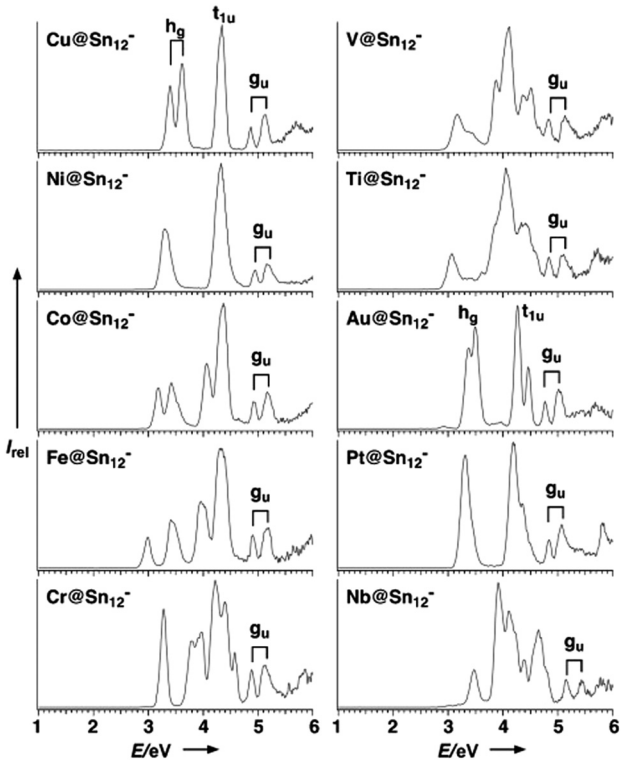

Fig. 9 Photoelectron spectra (PES) of gas-phase species $[M@Sn_{12}]^-$ at 193 nm (6.424 eV). The signals that stem from the three highest occupied orbitals (h_g, t_{1u}, g_u) are depicted; note that the 1– charge of these clusters does not necessarily represent the original charge of the species in the condensed phase, as they easily undergo oxidation reactions in the gas phase. This figure has been reproduced from ref. 39 with permission from Wiley-VCH, copyright 2007.

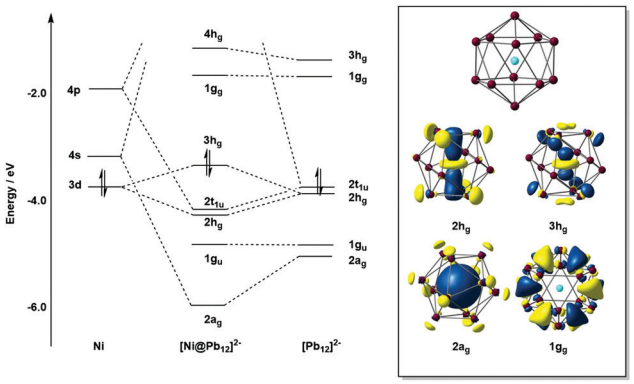

Fig. 10 Molecular orbital (MO) diagram for the Ni atom, icosahedral $[Ni@Pb_{12}]^{2-}$, and Pb_{12}^{2-}, computed using DFT. The diagram illustrates the strong similarity between the eigenvalues of the cluster and those of the parent (empty) Pb_{12}^{2-} cage, except for the $3h_g$ (HOMO) and $2a_g$ orbitals.

inevitably favour approximately spherical arrangements of atoms over non-centrosymmetric isomers where one face is exposed. We have noted similar trends in the structural chemistry of $[An@Bi_{12}]^{4-}$ compared to empty 'Bi_{12}^{8-}', where the presence of a central metal ion favours a more compact geometry that maximises electrostatic attractions. A rare example of a genuinely endohedral cluster with a *nido* geometry is the C_{5v}-symmetric $[Ag@Pb_{11}]^{3-}$ (Fig. 11) with a total electron count of 48 (= $4n + 4$).[175] The structure shows the classic open face typical of this electron count and, although Cu and Au analogues have not been isolated, they have been proposed as intermediates in the growth of larger clusters such as $[Cu_4Pb_{22}]^{4-}$, $[Au_8Pb_{33}]^{6-}$ and $[Au_{12}Pb_{44}]^{8-}$.[175]

A number of recent examples from the 12-vertex family with which we are primarily concerned in this review highlight the tendency to retain centrosymmetric geometries despite having electron counts that would be consistent with *nido* geometries.[169,176–178] The $[Au@Pb_{12}]^{3-}$ cluster is a particularly interesting example:[176] if we assume that the Au 5d electrons do not contribute to the total electron count, the skeletal electron count of 52 = $4n + 4$ suggests that a *nido* geometry should be adopted, just as it is for $[Ag@Pb_{11}]^{3-}$. Instead, the X-ray structure reveals a highly distorted icosahedron, compressed along one C_3 axis to give D_{3d}-symmetry (Fig. 12, top right). The HOMO of $[Au@Pb_{12}]^{3-}$ (with a_{2g} symmetry in the D_{3d}-symmetric structure, see Fig. 13) has zero amplitude on the Au 6s, 5d or 6p orbitals, and its nodal characteristics are identical to those of one component of the g_g-symmetric LUMO of $[Ni@Pb_{12}]^{2-}$ shown in Fig. 10. This shows that the additional 2 electrons, above and beyond the 50-electron *closo* count, occupy an orbital localised on the Pb_{12} cage, and suggests that the most appropriate formulation of this cluster is $[Au^+@Pb_{12}^{4-}]^{3-}$. The driving force for the observed compression along a 3-fold axis of the icosahedron is then a first-order Jahn–Teller instability within the g_g^2 configuration.

The fact that $[Ag@Pb_{11}]^{3-}$ favours a *nido* structure while $[Au@Pb_{12}]^{3-}$ prefers a distorted icosahedron, despite both having classically *nido* electron counts of $4n + 4$, probably reflects the absence of a highly symmetric '*closo*' E_{11} geometry

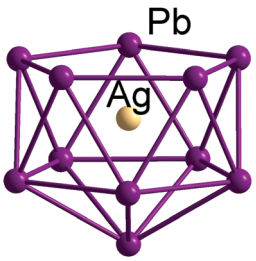

Fig. 11 Molecular structure of the *nido*-type endohedral Zintl cluster $[Ag@Pb_{11}]^{3-}$.[175]

analogous to the icosahedron. A closely-related example of a distorted icosahedron, the $[Co@Ge_{12}]^{3-}$ anion, merits comment in this context (Fig. 12, bottom left).[177] Despite having exactly the same 50-electron (*closo*) count as perfectly icosahedral $[M@Pb_{12}]^{2-}$ (M = Ni, Pd, Pt), the icosahedron in $[Co@Ge_{12}]^{3-}$ is significantly elongated along one 5-fold axis. Sun, Boldyrev and co-workers argued that size drives this distortion: the (formally negatively charged) Co atom is simply too large to fit inside the cavity of a Ge_{12}^{2-} icosahedron. Alternatively, a second-order Jahn–Teller instability caused by the energetic proximity of the metal 3d orbitals (h_g symmetry in an icosahedron) and the g_g LUMO of the Ge_{12}^{2-} cage can drive a lowering of symmetry to D_{5d} which allows the flow of electron density from four of the metal 3d orbitals into the four components of the LUMO of the cage (now a pair of e_{1g}-symmetric orbitals) (Fig. 14). The relationship to $[Ru@Ge_{12}]^{3-}$, which was discussed in the context of electron-precise clusters, is significant here: the driving force for transfer of electron density outwards from the metal d orbitals to the cage is, in $[Co@Ge_{12}]^{3-}$, sufficient to distort the icosahedron *via* 2nd order Jahn–Teller effects, but not sufficient to force a wholesale rearrangement to the 3-connected architecture found

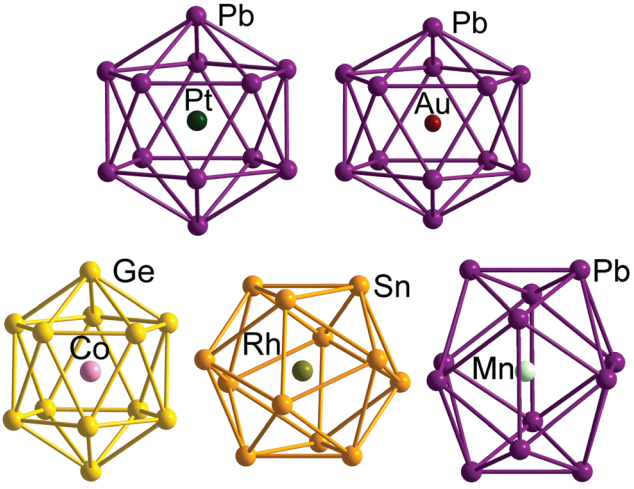

Fig. 12 Structure of the undistorted endohedral Zintl cluster $[Pt@Pb_{12}]^{2-}$ with 50 = ***4n*** + **2** valence electrons (top left)[158] compared to other $[M@E_{12}]^{q-}$ clusters that do exhibit distorted, yet still near-icosahedral structures: Au/Pb/3 (***4n*** + **4** electrons, D_{3d} symmetry, top right),[176] Co/Ge/3 (***4n*** + **2** *electrons*, approximate D_{5d} symmetry, bottom right),[177] Rh/Sb/3 (***4n*** + **2** electrons, D_{3d}-symmetry, bottom centre),[169] Mn/Pb/3 (***4n*** − **2** electrons, D_{2h} symmetry, bottom left).[178]

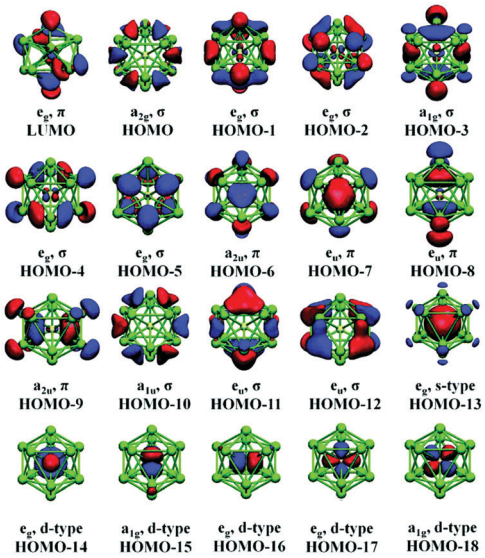

Fig. 13 Canonical orbitals calculated for $[Au@Pb_{12}]^{3-}$ by means of DFT methods. Only one of the twofold degenerate LUMO orbitals are drawn. This figure has been reproduced from ref. 176 with permission from RSC, copyright 2017.

in $[Ru@Ge_{12}]^{3-}$. The greater availability (in both spatial and energetic senses) of the 4d orbitals of Ru compared to the 3d orbitals of Co is therefore the key driver for the different cluster geometries of $[Co@Ge_{12}]^{3-}$ and $[Ru@Ge_{12}]^{3-}$. An extension of this argument also allows us to rationalise the striking D_{2h}-symmetric distortion observed in $[Mn@Pb_{12}]^{3-}$, which is elongated along one 2-fold rotation axis of the icosahedron (Fig. 12, bottom right).[178] $[Mn@Pb_{12}]^{3-}$ can be formulated as $[Mn^{-}@Pb_{12}^{2-}]^{3-}$ and the (high-spin) d^8 configuration at Mn can be stabilised by allowing electron transfer from the spin-β components of the three doubly occupied Mn 3d orbitals to the (g_g) LUMO of cage. The favoured distortion is therefore one which stabilises precisely three, rather than four, of the components of the g_g-symmetric LUMO of the icosahedron, and this is precisely the situation engineered by the elongation along a 2-fold axis (Fig. 14, right). In the limit that one spin-β electron was transferred entirely to each of the three stabilised components of the cage LUMO, the Mn atom would achieve a stable half-filled (d^5) configuration and the effective electron count at the cage would increase to 53. The common theme that unites the structural chemistry of this trio of clusters is therefore the flow of electrons from metal to the 4-fold degenerate LUMO of the icosahedral cage, whether it be driven by 1st-order Jahn–Teller instabilities ($[Au@Pb_{12}]^{3-}$), 2nd-order Jahn–Teller instabilities ($[Co@Ge_{12}]^{3-}$), or the stability of the half-filled d shell on the metal ($[Mn@Pb_{12}]^{3-}$). A summary of the distortions, along with the corresponding changes in the frontier orbitals, is given in Fig. 14. Although this spectrum of bonding situations is most well characterised within the 12-vertex family, the same pattern of increasing participation of metal d electron density can also be identified in the 10-vertex analogues $[Ni@Pb_{10}]^{2-}$, marginally distorted but still deltahedral $[Fe@Sn_{10}]^{3-}$ and the 3-connected $[Co@Ge_{10}]^{3-}$ cluster discussed above.

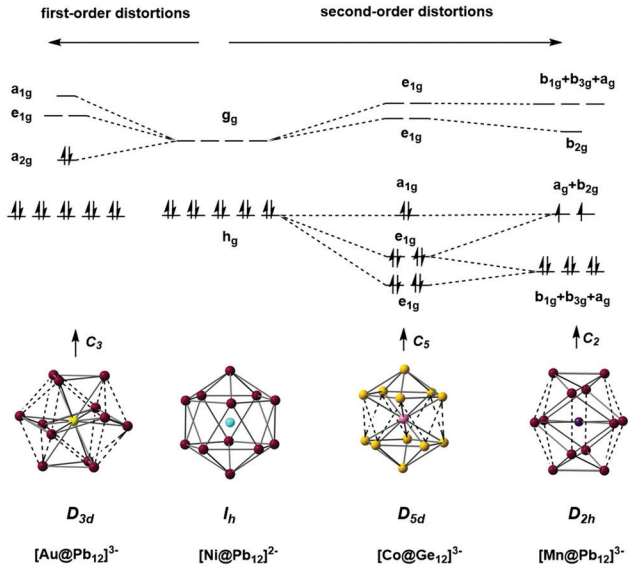

Fig. 14 The origin of distortions in approximately icosahedral clusters $[Ni@Pb_{12}]^{2-}$, $[Au@Pb_{12}]^{3-}$, $[Co@Ge_{12}]^{3-}$, and $[Mn@Pb_{12}]^{3-}$.

There remains one further arrangement of 12 atoms in an electron deficient polyhedron around a single endohedral atom, the ternary cluster anion $[Co@Sn_6Sb_6]^{3-}$ (Fig. 15)[179] where two face-sharing square antiprisms form a $(Sn_6Sb_6)^{2-}$ cluster shell that encapsulates one Co^- in one of the square antiprisms (the lower one in Fig. 15). The lower square antiprism is significantly expanded to accommodate the Co atom, such that the distances between the lower and middle squares (3.45 Å on average) are at least 0.4 Å larger than all other interatomic distances (on average: 3.06 Å between the upper and middle square, 3.14 within the middle square, 2.87 Å within the upper and lower squares).

The Co centre could, therefore, also be regarded as 8-coordinate in a square antiprismatic array defined by two 4-membered rings, one of which is shared with the residual unbound Sn_2Sb_2 square. This binary $(Sn_6Sb_6)^{2-}$ shell has an electron count of 56 electrons, so either $4n + 8$ or $5n - 4$, depending on whether we choose to start from the electron-deficient or electron-precise limit. The cluster shows characteristics of both the $4n$ and the $5n$ limits, with both deltahedral and square faces. The intermediate electron count of 56 means that neither the icosahedron characteristic of 50-electron $[M@Pb_{12}]^{2-}$ nor the 3-connected architecture adopted by 60-electron $[Ta@Ge_8As_4]^{3-}$ are viable structural choices. The division of the $(Sb_6Sn_6)^{2-}$ cluster into a 38-electron, 8-vertex arachno $(Sb_4Sn_4)^{2-}$ unit and a planar 18-electron Sb_2Sn_2 unit which is a 2π electron aromatic, isolobal with $(C_4H_4)^{2+}$, then partitions the electron density in such a way that two stable units emerge. An argument in favour of this interpretation is the fact that, if all eight atoms contribute 2 electrons to the Co–(Sn, Sb) interactions, the Co atom would adopt an 18-electron noble-gas configuration. However, as related clusters exist where two Co^- ions or two Ni atoms are accommodated in both hemispheres of the 12-vertex shell, which are more regular in shape, one can also think of a special kind of an endohedral cluster without partition into said substructures. Detailed DFT studies of the total electron count actually indicate that the architecture behaves like a closely interconnected assembly of 12 atoms: when adding electrons (by replacing Sn with Sb atoms), the cluster shell as a whole undergoes deformation.

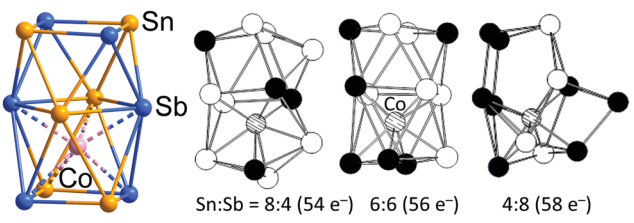

Fig. 15 Structure of the $[Co@Sn_6Sb_6]^{3-}$ cluster (left), and illustration of the effect of decreasing or increasing electron numbers on the structure of the 12-vertex cluster shell (DFT; centre and right). This figure has been adopted from ref. 179 with permission from Wiley-VCH, copyright 2018.

To summarize the essence of Chapters 4.1–4.3, we emphasize that – like Zintl anions without an endohedral guest – endohedral Zintl clusters can be understood as belonging to one large family, the structural characteristics of which are dominated by the total valence electron count of the cluster shell. There is thus no general difference in how to interpret clusters that have valence electron counts between $4n$ and $5n$ or between $5n$ and $6n$; it is necessary only to understand how the clusters manage an excess/deficit of electrons relative to the ideal number of $5n$ for a spherical, highly symmetrical cluster with three-bonded atoms. Highly symmetric clusters are reached at the bottom or top of the 'ladder' of possible electron counts (except for the minimum number being $4n + 2$ instead of $4n$ due to the presence of the strongly bonding totally symmetric MO that is common to all). The crucial question, which tips the scales, is how the endohedral d-block or f-block atom interacts with the p-block metal shell, and whether the electrons in these shells contribute to the overall electron count or not. Unlike the boranes (and most of the known Zintl anions), endohedral Zintl clusters tend to retain centrosymmetric *closo*-like structures despite having *nido*-like or even higher electron counts, as a result of the spherically symmetric potential imposed by the atom at the centre of the cluster. This point marks the most significant difference between endohedral and non-endohedral clusters, but thorough analyses of the electronic structures are usually essential to rationalise a given structural preference.

4.4 Steps towards cluster growth: fused clusters

The very extensive chemistry of boranes based on two or more fused *closo* polyhedra is not mirrored in the Zintl-ion domain, where there are still relatively few examples of fused cluster units. The dearth of these larger clusters probably reflects the coulomb explosion associated with the linking of subunits which typically carry a high negative charge. Amongst those that are known, the majority contain closed-shell (d^{10}) transition metal ions that are well separated from each other, with little or no potential for metal–metal bonding. Examples of clusters of this type include $[Co_2@Ge_{16}]^{4-}$,[180] $[M_2@Sn_{17}]^{4-}$ (M = Ni, Pt)[181,182] or $[Pd_2@Tt_{18}]^{4-}$ (Tt = Ge, Sn),[183,184] based on

the vertex sharing of two Sn_9 units, the C_{3v}-symmetric $[Rh_3@Sn_{24}]^{5-}$ cluster where three Sn_9 units share common edges around a central trigonal prism, and $[Au_3Ge_{45}]^{9-}$ that has the same (idealized) symmetry, yet is based on four Ge_9^{4-} units, one of which is extended to an unusual Ge_{18} unit.[185] The ideas that underpin the Wade-Mingos rules have been extended to clusters containing two or more fused deltahedral units through Jemmis' 'mno' rules that include the impact of fusion *via* vertices, edges or faces.[70,71] The same ideas can also be applied to the fused Zintl-ion clusters: the $[Ni_2Sn_{17}]^{4-}$ cluster, for example, can be rationalised in terms of a total count of $2(m + n + o) = 40$, where m is the number of condensed polyhedra (2), n the number of vertices (17) and o the number of shared single vertices (1). It is important to emphasise, however, that NMR studies have shown that Zintl-ion clusters (whether with one or more endohedral metal ions) are typically very fluxional, suggesting a rather flat potential energy surface connecting multiple minima. This, along with the very high negative charges associated with the ions, means that the cationic lattice may exert a very substantial influence on structure (so-called 'packing effects' in the crystal). In such circumstances, it is not obvious that a direct correlation between structure and the intrinsic electron count of the isolated anion should be expected. In addition to the examples where the transitions metal ions are effectively 'dilute' (which led to the alternative terminology of 'intermetalloid clusters')[32] there is a small number of examples where direct metal–metal bonding cannot be neglected. In the majority of these cases, transition metal ions occupy vertices of the polyhedral as well as the endohedral sites, allowing them to bridge multiple polyhedral. The $[Ni_3@Ge_{18}]^{4-}$ cluster reported by Sevov and Goicoechea is a prominent example of this kind, with a linear Ni_3 chain and Ni–Ni distances of 2.49 Å.[186]

5. Conclusions and outlook

In this article we have tried to bring together a diverse body of structural data to identify the underlying patterns and trends that drive structural change as a function of electron count. In so doing, we encounter a wide range of bond types, from localised 2c–2e bonding in electron-precise clusters through to highly delocalised multi-centre bonds in their more electron-deficient counterparts. Rather different theoretical paradigms are typically applied to these distinct scenarios, and we have tried to cut through these distinctions to reveal relationships between apparently rather different cluster species. Perhaps the most critical issue is the role of the electrons on the endohedral metal: at one limit they can be entirely core-like while at the other they can interact strongly with the orbitals on the shell, effectively raising the cluster electron count. Thus a careful consideration of the role of the metal d or f electrons is critical to understanding the structural diversity within this family.

Our emphasis has been primarily on the 12-vertex family, simply because this offers the greatest diversity. Within this family we find numerous examples of icosahedral cages characteristic of multi-centre bonding, low (50) electron counts and essentially core-like metal d electrons. At the opposite extreme, electron-poor transition metal atoms such as Ta contribute all of their valence electrons to the cage to give a total count of 60, driving the adoption of 3-connected structures that are more characteristic of electron precise counts and 2c–2e bonding. The cases that fall between these limits are perhaps the most fascinating of all: the cluster can accommodate changes in electron count either through subtle distortions of the icosahedron, or, in more extreme cases, by sub-dividing the 12-vertex cluster into electronically distinct sub-units. For electron counts above 60, the structural trends can be understood in a localized context, where successive 2-electron increments in the count drive the cleavage of bonds and hence the adoption of structures with 2-connected vertices.

Perhaps the most important point that emerges from this survey is that the structural chemistry of this seemingly unconnected set of compounds can be understood within a single continuous framework defined by the total electron count at the cluster (shell). Unlike the boranes or empty Zintl ions, however, the electron count is not always *a priori* obvious—it depends critically on the characteristics of the transition metal or f-block element at the centre of the cluster. Capturing these characteristic properties of d- and f-electrons presents a very substantial challenge to theory, and it should therefore come as little surprise that the structural predictions in this field are often highly dependent on choice of methodology. This dependence highlights the importance of trends and patterns in data rather than isolated data points – only when we consider the body of data as a whole can we truly appreciate the connections that unify the field.

This article is dedicated to Professor D. M. P. Mingos in recognition of his extraordinary contributions to the field of cluster chemistry, and in particular in identifying the links between electronic and geometric structure.

Conflicts of interest

There are no conflicts to declare.

Acknowledgements

This work was supported by the German Research Society (Deutsche Forschungsgemeinschaft, DFG) and the Alexander von Humboldt Foundation.

Notes and references

1 *Metal Clusters*, ed. W. Ekardt, John Wiley & Sons Ltd, 1st edn, 1999.
2 *Metal Clusters in Chemistry*, ed. P. Braunstein, L. A. Oro and P. R. Raithby, Wiley-VCH, 1st edn, 1999.
3 T. Tsukuda and H. Häkkinen, *Front. Nanosci*, 2015, **9**, 1–7.
4 T. P. Fehlner, in *Cluster Compounds: Inorganometallic Compounds Containing Transition Metal & Main Group Elements,*

in Encyclopedia of Inorganic Chemistry, ed. R. B. King, R. H. Crabtree, C. M. Lukehart, D. A. Atwood and R. A. Scott, 2006, DOI: 10.1002/0470862106.ia097.
5 F. Weigend and R. Ahlrichs, *Phil. Trans. R. Soc. A*, 2010, **368**, 1245–1263.
6 Clusters – Contemporary Insight in Structure and Bonding, in *Structure and Bonding*, ed. S. Dehnen, Springer, 1st edn, 2017.
7 P. Braunstein and A. A. Danopoulos, *Chem. Rev.*, 2021, **121**, 7346–7397.
8 S. Takano and T. Tsukuda, *J. Am. Chem. Soc.*, 2021, **143**, 1683–1698.
9 T. Tsukamoto, T. Kambe, T. Imaoka and K. Yamamoto, *Nat. Rev. Chem*, 2021, **5**, 338–347.
10 A. Purath, R. Köppe and H. Schnöckel, *Angew. Chem., Int. Ed.*, 1999, **38**, 2926–2928.
11 A. Schnepf and H. Schnöckel, *Angew. Chem., Int. Ed.*, 2002, **41**, 3532–3554.
12 H. Schnöckel, *Chem. Rev.*, 2010, **110**, 4125–4163.
13 C. Döring, A.-M. Dietel, M. V. Butovskii, V. Bezugly, F. R. Wagner and R. Kempe, *Chem. – Eur. J*, 2010, **16**, 10679–10683.
14 S. Gonzalez-Gallardo, G. Prabusankar, T. Cadenbach, C. Gemel, M. von Hopffgarten, G. Frenking and R. A. Fischer, *Struct. Bond.*, 2010, **136**, 147–188.
15 S. Scharfe, F. Kraus, S. Stegmaier, A. Schier and T. F. Fässler, *Angew. Chem., Int. Ed.*, 2011, **50**, 3630–3670.
16 Zintl Phases – Principles and Recent Developments, in *Structure and Bonding*, ed. T. F. Fässler, Springer, 1st edn, 2011.
17 S. González-Gallardo, T. Bollermann, R. A. Fischer and R. Murugavel, *Chem. Rev.*, 2012, **112**, 3136–3170.
18 B. Oelkers, M. V. Butovskii and R. Kempe, *Chem. – Eur. J*, 2012, **18**, 13566–13579.
19 B. Weinert and S. Dehnen, *Struct. Bond.*, 2017, **174**, 99–134.
20 K. Mayer, J. Weßing, T. F. Fässler and R. A. Fischer, *Angew. Chem., Int. Ed.*, 2018, **57**, 14372–14393.
21 B. Weinert, S. Mitzinger and S. Dehnen, *Chem. – Eur. J.*, 2018, **24**, 8470–8490.
22 R. J. Wilson, B. Weinert and S. Dehnen, *Dalton Trans*, 2018, **47**, 14861–14869.
23 B. Peters, N. Lichtenberger, E. Dornsiepen and S. Dehnen, *Chem. Sci*, 2020, **11**, 16–26.
24 R. E. Benfield, D. Grandjean, M. Kröll, R. Pugin, T. Sawitowski and G. Schmid, *J. Phys. Chem. B*, 2001, **105**, 1961–1970.
25 M. M. Bentlohner, M. Waibel, P. Zeller, K. Sarkar, P. Müller-Buschbaum, D. Fattakhova-Rohlfing and T. F. Fässler, *Angew. Chem., Int. Ed.*, 2016, **55**, 2441–2445.
26 Z. Luo, A. W. Castleman, Jr. and S. N. Khanna, *Chem. Rev.*, 2016, **116**(23), 14456–14492.
27 P. Ferrari, J. Vanbuel, E. Janssens and P. Lievens, *Acc. Chem. Res.*, 2018, **51**, 3174–3182.
28 Y.-X. Zhao, Z.-Y. Li, Y. Yang and S.-G. He, *Acc. Chem. Res.*, 2018, **51**, 2603–2610.
29 O. P. E. Townrow, C. Chung, S. A. Macgregor, A. S. Weller and J. M. Goicoechea, *J. Am. Chem. Soc.*, 2020, **142**, 18330–18335.
30 C. Dong, Y. Li, D. Cheng, M. Zhang, J. Liu, Y.-G. Wang, D. Xiao and D. Ma, *ACS Catalysis*, 2020, **10**, 11011–11045.
31 G.-L. Hou, E. Faragó, D. Buzsáki, L. Nyulászi, T. Höltzl and E. Janssens, *Angew. Chem., Int. Ed.*, 2021, **60**, 4756–4763.
32 T. F. Fässler and S. D. Hoffmann, *Angew. Chem., Int. Ed.*, 2004, **43**, 6242–6247.
33 J. M. Goicoechea and J. E. McGrady, *Dalton Trans*, 2015, **44**, 6755–6766.
34 X. Jin, V. Arcisauskaitea and J. E. McGrady, *Dalton Trans*, 2017, **46**, 11636–11644.
35 X. Jin and J. E. McGrady, *Adv. Inorg. Chem.*, 2019, **73**, 265–304.
36 R. J. Wilson, N. Lichtenberger, B. Weinert and S. Dehnen, *Chem. Rev.*, 2019, **119**, 8506–8554.
37 J. Zhao, Q. Du, S. Zhou and V. Kumar, *Chem. Rev.*, 2020, **120**, 9021–9163.
38 J. P. Dognon, C. Clavaguéra and P. Pyykkö, *Angew. Chem., Int. Ed.*, 2007, 46, 1427–1430.
39 L.-F. Cui, X. Huang, L.-M. Wang, J. Li and L.-S. Wang, *Angew. Chem., Int. Ed.*, 2007, **46**, 742–745.
40 A. Grubisic, Y. J. Ko, H. Wang and K. H. Bowen, *J. Chem. Phys.*, 2008, **129**, 054302.
41 A. Grubisic, Y. J. Ko, H. Wang and K. H. Bowen, *J. Am. Chem. Soc.*, 2009, **131**, 10783–10790.
42 A. Grubisic, H. Wang, X. Li, Y.-J. Ko, F. S. Kocak, M. Pederson, K. Bowen and B. Eichhorn, *Proc. Natl. Acad. Sci. U. S. A.*, 2011, **108**, 14757–14762.
43 H. G. Xu, X. Y. Kong, X. J. Deng, Z. G. Zhang and W. J. Zheng, *J. Chem. Phys.*, 2014, **140**, 024308.
44 X. J. Deng, X. Y. Kong, H. G. Xu, X. L. Xu, G. Feng and W. J. Zheng, *J. Phys. Chem. C*, 2015, **119**, 11048–11055.
45 X. J. Li, P. Claes, M. Haertelt, P. Lievens, E. Janssens and A. Fielicke, *Phys. Chem. Chem. Phys.*, 2016, **18**, 6291–6300.
46 S. J. Lu, L. R. Hu, X. L. Xu, H. G. Xu, H. Chen and W. J. Zheng, *Phys. Chem. Chem. Phys.*, 2016, **18**, 20321–20329.
47 X. J. Deng, X. Y. Kong, X. Q. Liang, B. Yang, H. G. Xu, X. L. Xu, G. Feng and W. J. Zheng, *J. Chem. Phys.*, 2017, **147**, 234310.
48 X. Q. Liang, X. J. Deng, S. J. Lu, X. M. Huang, J. J. Zhao, H. G. Xu, W. J. Zheng and X. C. Zeng, *J. Phys. Chem. C*, 2017, **121**, 7037–7046.
49 H. Tsunoyama, H. Akatsuka, M. Shibuta, T. Iwasa, Y. Mizuhata, N. Tokitoh and A. Nakajima, *J. Phys. Chem. C*, 2017, **121**, 20507–20516.
50 M. Shibuta, T. Niikura, T. Kamoshida, H. Tsunoyama and A. Nakajima, *Phys. Chem. Chem. Phys.*, 2018, **20**, 26273–26279.
51 H. G. Yang, X. L. Xu, W. J. Xu and J. Zheng, *J. Phys. Chem. A*, 2018, **122**, 9886–9893.
52 V. Fries, M. P. Klein, A. Steiner, M. H. Prosenc and G. Niedner-Schatteburg, *Phys. Chem. Chem. Phys.*, 2021, **23**, 11345–11354.
53 E. N. Esenturk, J. Fettinger, Y.-F. Lam and B. Eichhorn, *Angew. Chem., Int. Ed.*, 2004, **43**, 2132–2134.
54 P. Villard, *C. R. Hebd. Seances Acad. Sci.*, 1896, **123**, 377.

55 R. de Forcrand, *C. R. Hebd. Seances Acad. Sci.*, 1923, **176**, 355.
56 R. de Forcrand, *C. R. Hebd. Seances Acad. Sci.*, 1923, **181**, 15.
57 D. Londono, W. F. Kuhs and J. L. Finney, *Nature*, 1988, **332**, 141.
58 H. C. Longuet-Higgins and R. P. Bell, *J. Chem. Soc.*, 1943, 250–255.
59 K. Wade, *J. Chem. Soc. D*, 1971, 792–793.
60 D. M. P. Mingos, *Nat. Phys. Sci.*, 1972, **236**, 99–102.
61 K. Wade, *Adv. Inorg. Chem. Radiochem.*, 1976, **18**, 1–66.
62 W. N. Lipscomb, *Science*, 1977, **196**, 1047–1055.
63 D. M. P. Mingos, *J. Chem. Soc., Chem. Commun.*, 1983, 706–708.
64 D. M. P. Mingos and D. G. Evance, *J. Organometal. Chem*, 1983, **251**, C13–C16.
65 D. M. P. Mingos, *Acc. Chem. Res.*, 1984, **17**, 311–319.
66 D. M. P. Mingos and J. Modrego, *New J. Chem*, 1991, **15**, 9–16.
67 D. M. P. Mingos, *Pure Appl. Chem.*, 1991, **63**, 807–812.
68 D. M. P. Mingos, *Chimia*, 2019, **73**, 152–164.
69 D. M. P. Mingos and D. J. Wales, *Introduction to Cluster Chemistry*, Prentice Hall, Englewood Cliffs, New Jersey, 1990.
70 E. D. Jemmis, M. M. Balakrishnarajan and P. D. Pancharatna, *J. Am. Chem. Soc.*, 2001, **123**, 4313–4323.
71 E. D. Jemmis, M. M. Balakrishnarajan and P. D. Pancharatna, *Chem. Rev.*, 2002, **102**, 93–144.
72 R. Hoffmann, *J. Chem. Phys.*, 1963, **39**, 1397–1412.
73 M. Brack, *Rev. Mod. Phys.*, 1993, **65**, 677–732.
74 Z. Lin, T. Slee and D. M. P. Mingos, *Chem. Phys.*, 1990, **142**, 321–334.
75 W. A. de Heer, W. D. Knight, M. Y. Chou and M. L. Cohen, *Solid State Phys*, 1987, **40**, 93–182.
76 A. W. Castleman, Jr. and S. N. Khanna, *J. Phys. Chem. C*, 2009, **113**(7), 2664–2675.
77 P. Jena, *J. Phys. Chem. Lett.*, 2013, **4**, 1432–1442.
78 T. Iwasa and A. Nakajima, *J. Phys. Chem. C*, 2013, **117**, 21551–21557.
79 X. Z. Luo and A. W. Castleman, *Acc. Chem. Res.*, 2014, **47**, 2931–2940.
80 J. U. Reveles, P. A. Clayborne, A. C. Reber, S. N. Khanna, K. Pradhan, P. Sen and M. R. Pederson, *Nat. Chem*, 2009, **1**, 310–315.
81 D. A. Tomalia and S. N. Khanna, *Chem. Rev.*, 2016, **116**, 2705–2774.
82 A. C. Reber and S. N. Khanna, *Acc. Chem. Res.*, 2017, **50**, 255–263.
83 A. R. Eulenstein, Y. J. Franzke, N. Lichtenberger, R. J. Wilson, L. Deubner, F. Kraus, R. Clérac, F. Weigend and S. Dehnen, *Nat. Chem*, 2021, **13**, 149–155.
84 A. R. Eulenstein, Y. J. Franzke, P. Bügel, W. Massa, F. Weigend and S. Dehnen, *Nat. Commun.*, 2020, **11**, 5122.
85 R. G. Parr and W. Yang, *Density Functional Theory of Atoms and Molecules*, Oxford University Press, New York, 1988.
86 B. O. Roos, P. R. Taylor and P. E. M. Sigbahn, *Chem. Phys.*, 1980, **48**, 157–173.
87 A. D. Becke, *Phys. Rev. A: At., Mol., Opt. Phys.*, 1988, **38**, 3098–3100.
88 J. P. Perdew, *Phys. Rev. B: Condens. Matter Mater. Phys.*, 1986, **33**, 8822–8824.
89 J. P. Perdew, K. Burke and M. Ernzerhof, *Phys. Rev. Lett.*, 1996, **77**, 3865–3868.
90 C. Lee, W. Yang and R. G. Parr, *Phys. Rev. B: Condens. Matter Mater. Phys.*, 1988, **37**, 785–789.
91 J. P. Perdew, M. Ernzerhof and K. Burke, *J. Chem. Phys.*, 1996, **105**, 9982–9985.
92 J. Tao, J. P. Perdew, V. N. Staroverov and G. E. Scuseria, *Phys. Rev. Lett.*, 2003, **91**, 146401.
93 V. N. Staroverov, G. E. Scuseria, J. Tao and J. P. Perdew, *J. Chem. Phys.*, 2003, **119**, 12129.
94 P. Pyykkö, *Chem. Rev.*, 1988, **88**, 563–594.
95 X. Cao and M. Dolg, *Chem Rev*, 2012, **112**, 403–480.
96 W. Kutzelnigg and W. Liu, *J. Chem. Phys.*, 2005, **123**, 241102.
97 Y. J. Franzke and F. Weigend, *J. Chem Theory Comput*, 2019, **15**, 1028–1043.
98 Y. J. Franzke, F. Mack and F. Weigend, *J. Chem. Theory Comput.*, 2021, **17**, 3974–3994.
99 A. Klamt and G. Schüürmann, *J. Chem. Soc., Perkin Trans.*, 1993, **2**, 799–805.
100 M. Bühl and A. Hirsch, *Chem. Rev.*, 2001, **101**, 1153–1184.
101 E. Hückel, *Z. Phys*, 1931, **70**, 204–286.
102 T. Koopmans, *Physica*, 1934, **1**, 104–113.
103 S. F. Boys, *Rev. Mod. Phys.*, 1960, **32**, 296–299.
104 J. Pipek and P. G. Mezey, *J. Chem. Phys.*, 1989, **90**, 4916–4926.
105 W. Kutzelnigg, *Einführung in die Theoretische Chemie*, Wiley-VCH, 2002, vol. 2, pp. 210–211.
106 A. E. Reed, R. B. Weinstock and F. Weinhold, *J. Chem. Phys.*, 1985, **83**, 735–846.
107 D. Y. Zubarev and A. I. Boldyrev, *Phys. Chem. Chem. Phys.*, 2008, **10**, 5207–5217.
108 D. Sundholm, H. Fliegl and R. J. Berger, *Wiley Interdiscip. Rev. Comput. Mol. Sci*, 2016, **6**, 639–678.
109 A. D. McNaught and A. Wilkinson, *Compendium of Chemical Terminology*, ed. S. J. Chalk, Blackwell Scientific Publications, 2nd edn, 1997, online version 2019.
110 P. v. R. Schleyer, C. Maerker, A. Dransfeld, H. Jiao and N. Hommes, *J. Am. Chem. Soc.*, 1996, **118**, 6317–6318.
111 C. Liu, I. Popov, Z. Chen, A. Boldyrev and Z. Sun, *Chem. – Eur. J.*, 2018, **24**, 14583–14597.
112 I. F. Hewaidy, E. Busmann and W. Klemm, *Z. Anorg. Allg. Chem.*, 1964, **328**, 283–293.
113 H.-L. Xu, I. A. Popov, N. V. Tkachenko, Z.-C. Wang, A. Muñoz-Castro, A. I. Boldyrev and Z.-M. Sun, *Angew. Chem., Int. Ed.*, 2020, **59**, 17286–17290.
114 C. B. Benda, M. Waibel, T. Köchner and T. F. Fässler, *Chem. – Eur. J*, 2014, **20**, 16738–16746.
115 S. C. Critchlow and J. D. Corbett, *Inorg. Chem.*, 1982, **21**, 3286–3290.
116 S. C. Critchlow and J. D. Corbett, *Inorg. Chem.*, 1985, **24**, 979–981.

117 G. Cordier and W. Blase, *Z. Kristallogr.*, 1991, **196**, 207–211.
118 L. Xu and S. C. Sevov, *Inorg. Chem.*, 2000, **39**, 5383–5389.
119 F. Lips, I. Schellenberg, R. Pöttgen and S. Dehnen, *Chem. – Eur. J*, 2009, **15**, 12968–12973.
120 R. Ababei, J. Heine, M. Holyńska, G. Thiele, B. Weinert, X. Xie, F. Weigend and S. Dehnen, *Chem. Commun.*, 2012, **48**, 11295–11297.
121 S. Mitzinger, L. Broeckaert, W. Massa, F. Weigend and S. Dehnen, *Nat. Commun.*, 2016, **7**, 10480–10490.
122 S. Mitzinger, J. Bandemehr, K. Reiter, J. S. McIndoe, X. L. Xie, F. Weigend, J. F. Corrigan and S. Dehnen, *Chem. Commun.*, 2018, **54**, 1421–1424.
123 F.-X. Pan, L.-J. Li and Z.-M. Sun, *Chin. J. Struct. Chem.*, 2016, **35**, 1099–1106.
124 F. Pan, L. Guggolz, F. Weigend and S. Dehnen, *Angew. Chem., Int. Ed.*, 2020, **59**, 16638–16643.
125 F. Weigend, C. Schrodt and R. Ahlrichs, *J. Chem. Phys.*, 2004, **121**, 10380–10384.
126 F. Weigend and C. Schrodt, *Chem. – Eur. J*, 2005, **11**, 3559–3564.
127 S. Bobev and S. C. Sevov, *Angew. Chem., Int. Ed.*, 2001, **40**, 1507–1510.
128 F.-X. Pan, L.-J. Li, Y.-J. Wang, J.-C. Guo, H.-J. Zhai, L. Xu and Z.-M. Sun, *J. Am. Chem. Soc.*, 2015, **137**, 10954–10957.
129 R. Ababei, W. Massa, K. Harms, X. Xie, F. Weigend and S. Dehnen, *Angew. Chem., Int. Ed.*, 2013, **52**, 13544–13548.
130 J. Barr, R. J. Gillespie, G. P. Pez, P. K. Ummat and O. C. Vaidya, *J. Am. Chem. Soc.*, 1970, **92**, 1081–1082.
131 C. Nicolas, G. Bernardinelli and J. Lacour, *J. Phys. Org. Chem.*, 2010, **23**, 1080–1087.
132 R. S. P. Turbervill and J. M. Goicoechea, *Chem. Rev.*, 2014, **114**, 10807–10828.
133 B. van IJzendoorn and M. Mehta, *Dalton Trans*, 2020, **49**, 14758–14765.
134 R. J. Wilson and S. Dehnen, *Angew. Chem., Int. Ed.*, 2017, **56**, 3098–3102.
135 F. Pan, S. Wei, L. Guggolz, A. Eulenstein, F. Tambornino and S. Dehnen, *J. Am. Chem. Soc.*, 2021, **143**, 7176–7188.
136 G. Espinoza-Quintero, J. C. A. Duckworth, W. K. Myers, J. E. McGrady and J. M. Goicoechea, *J. Am. Chem. Soc.*, 2014, **136**(4), 1210–1213.
137 B. Zhou, M. S. Denning, D. L. Kays and J. M. Goicoechea, *J. Am. Chem. Soc.*, 2009, **131**, 2802–2803.
138 J.-Q. Wang, S. Stegmaier and T. F. Fässler, *Angew. Chem., Int. Ed.*, 2009, **48**, 1998–2002.
139 A. Savin, O. Jepsen, J. Flad, O. K. Andersen, H. Preuss and H. G. von Schnering, *Angew. Chem., Int. Ed. Engl.*, 1992, **31**, 187–188.
140 X. Min, I. A. Popov, F.-X. Pan, L.-J. Li, E. Matito, Z.-M. Sun, L.-S. Wang and A. I. Boldyrev, *Angew. Chem., Int. Ed.*, 2016, **55**, 5531–5535.
141 N. Lichtenberger, R. J. Wilson, A. R. Eulenstein, W. Massa, R. Clérac, F. Weigend and S. Dehnen, *J. Am. Chem. Soc.*, 2016, **138**, 9033–9036.
142 B. Kesanli, J. Fettinger and B. Eichhorn, *Angew. Chem., Int. Ed.*, 2001, **40**, 2300–2302.
143 H.-G. von Schnering, J. Wok, D. Weber, R. Ramirez and T. Meyer, *Angew. Chem., Int. Ed. Engl.*, 1986, **25**, 353–354.
144 E. N. Esenturk, J. Fettinger and B. Eichhorn, *J. Am. Chem. Soc.*, 2006, **128**, 9178–9186.
145 B. Schiemenz and G. Huttner, *Angew. Chem., Int. Ed. Engl.*, 1993, **32**, 297–298.
146 J. M. Goicoechea and S. C. Sevov, *J. Am. Chem. Soc.*, 2004, **126**, 6860–6881.
147 J. Campbell and G. J. Schrobilgen, *Inorg. Chem.*, 1997, **36**, 4078–4081.
148 C. Suchentrunk and N. Korber, *New J. Chem.*, 2006, **30**, 1737–1739.
149 P. A. Edwards and J. D. Corbett, *Inorg. Chem.*, 1977, **16**, 903–907.
150 M. Somer, W. Carrillo-Cabrera, E. M. Peters, K. Peters, M. Kaupp and H. G. von Schnering, *Z. Anorg. Allg. Chem.*, 1999, **625**, 37–42.
151 Z. Dong and J. D. Corbett, *J. Am. Chem. Soc.*, 1994, **116**, 3429–3435.
152 Z.-C. Dong and J. D. Corbett, *Inorg. Chem.*, 1996, **35**, 3107–3112.
153 S. Ulvenlund, K. Stahl and L. Bengtsson-Kloo, *Inorg. Chem.*, 1996, **35**, 223–230.
154 J. M. Goicoechea and S. C. Sevov, *Inorg. Chem.*, 2005, **44**, 2654–2658.
155 C. H. E. Belin, J. D. Corbett and A. Cisar, *J. Am. Chem. Soc.*, 1977, **99**, 7163–7169.
156 J. Akerstedt, S. Ponou, L. Kloo and S. Lidin, *Eur. J. Inorg. Chem*, 2011, 3999–4005.
157 A. Spiekermann, S. D. Hoffmann and T. F. Fässler, *Angew. Chem., Int. Ed.*, 2006, **45**, 3459–3462.
158 D. Rios and S. C. Sevov, *Inorg. Chem.*, 2010, **49**(14), 6396–6398.
159 L.-F. Cui, X. Huang, L.-M. Wang, J. Li and L.-S. Wang, *J. Phys. Chem. A*, 2006, **110**(34), 10169–10172.
160 L.-F. Cui, X. Huang, L.-M. Wang, D. Y. Zubarev, A. I. Boldyrev, J. Li and L.-S. Wang, *J. Am. Chem. Soc.*, 2006, **128**, 8390–8391.
161 C. Seifried, L. Longo, P. Pollak and F. Weigend, *J. Chem. Phys.*, 2017, **146**, 034304.
162 M. Atoji and W. N. Lipscomb, *J. Chem. Phys.*, 1953, **21**, 172.
163 R. A. Jacobson and W. N. Lipscomb, *J. Am. Chem. Soc.*, 1958, **80**, 5571–5572.
164 M. B. Hursthouse, J. Kane and A. G. Massey, *Nature*, 1970, **228**, 659–660.
165 S. Kaskel and J. D. Corbett, *Inorg. Chem.*, 2000, **39**, 778–782.
166 S. C. Sevov and J. M. Goicoechea, *Organometallics*, 2006, **25**(24), 5678–5692.
167 S. Bobev and S. C. Sevov, *Angew. Chem., Int. Ed.*, 2000, **39**, 4108–4110.
168 E. N. Esenturk, J. Fettinger and B. Eichhorn, *Chem. Commun.*, 2005, 247–249.
169 C. Liu, X. Jin, L.-J. Li, J. Xu, J. E. McGrady and Z.-M. Sun, *Chem. Sci*, 2019, **10**, 4394–4401.
170 J.-Q. Wang, S. Stegmaier, B. Wahl and T. F. Fässler, *Chem. – Eur. J.*, 2010, **16**, 1793–1798.

171 Z. C. Dong and J. D. Corbett, *J. Am. Chem. Soc.*, 1995, **117**, 6447–6455.
172 B. J. L. Witzel, W. Klein, J. V. Dums, M. Boyko and T. F. Fässler, *Angew. Chem., Int. Ed.*, 2019, **58**, 12908–12913.
173 M. M. Gillett-Kunnath, J. I. Paik, S. M. Jensen, D. T. Jacob and S. C. Sevov, *Inorg. Chem.*, 2011, **50**, 11695–11701.
174 S. Scharfe, T. F. Fässler, S. Stegmaier, S. D. Hoffmann and K. Ruhland, *Chem. – Eur. J*, 2008, **14**, 4479–4483.
175 C.-C. Shu, H. W. T. Morgan, L. Qiao, J. E. McGrady and Z.-M. Sun, *Nat. Commun.*, 2020, **11**, 3477.
176 L.-J. Li, F.-X. Pan, F.-Y. Li, Z.-F. Chen and Z.-M. Sun, *Inorg. Chem. Front*, 2017, **4**, 1393–1396.
177 V. Liu, L.-J. Li, I. A. Popov, R. J. Wilson, C.-Q. Xu, J. Li, A. I. Boldyrev and Z.-M. Sun, *Chin. J. Chem*, 2018, **36**, 1165–1168.
178 B. Zhou, T. Krämer, A. L. Thompson, J. E. McGrady and J. M. Goicoechea, *Inorg. Chem.*, 2011, **50**, 8028–8037.
179 R. J. Wilson, F. Hastreiter, K. Reiter, P. Büschelberger, R. Wolf, R. Gschwind, F. Weigend and S. Dehnen, *Angew. Chem., Int. Ed.*, 2018, **57**, 15359–15363.
180 C. Liu, I. A. Popov, L. J. Li, N. Li, A. I. Boldyrev and Z. M. Sun, *Chem. – Eur. J*, 2018, **24**, 699–705.
181 E. N. Esenturk, J. C. Fettinger and B. W. Eichhorn, *J. Am. Chem. Soc.*, 2006, **128**(1), 12–13.
182 B. Kesanli, J. E. Halsig, P. Zavalij, J. C. Fettinger, Y.-F. Lam and B. W. Eichhorn, *J. Am. Chem. Soc.*, 2007, **129**(15), 4567–4574.
183 Jose M. Goicoechea and Slavi C. Sevov, *J. Am. Chem. Soc.*, 2005, **127**, 7676–7677.
184 Z.-M. Sun, H. Xiao, J. Li and L.-S. Wang, *J. Am. Chem. Soc.*, 2007, **129**, 9560–9561.
185 A. Spiekermann, S. D. Hoffmann, T. F. Fässler, I. Krossing and U. Preiss, *Angew. Chem., Int. Ed.*, 2007, **46**, 5310–5313.
186 J. M. Goicoechea and S. C. Sevov, *Angew. Chem., Int. Ed.*, 2005, **44**, 4026–4028.